Self-gating in semiconductor electrocatalysis

Yongmin He[1,2,13], Qiyuan He [1,13], Luqing Wang[3], Chao Zhu[1], Prafful Golani[1], Albertus D. Handoko[4], Xuechao Yu[2], Caitian Gao[2], Mengning Ding[5], Xuewen Wang[1], Fucai Liu[6], Qingsheng Zeng[1], Peng Yu[1], Shasha Guo[1], Boris I. Yakobson[3], Liang Wang[7], Zhi Wei Seh[4], Zhuhua Zhang[8], Minghong Wu[7], Qi Jie Wang [2,9]*, Hua Zhang[1,10]* and Zheng Liu[1,9,11,12]*

[1]School of Materials Science and Engineering, Nanyang Technological University, Singapore, Singapore. [2]Center for OptoElectronics and Biophotonics, School of Electrical and Electronic Engineering & The Photonics Institute, Nanyang Technological University, Singapore, Singapore. [3]Department of Materials Science and NanoEngineering, Rice University, Houston, TX, USA. [4]Institute of Materials Research and Engineering, Agency for Science, Technology and Research (A*STAR), Singapore, Singapore. [5]Key Laboratory of Mesoscopic Chemistry of MOE, School of Chemistry and Chemical Engineering, Nanjing University, Nanjing, China. [6]School of Optoelectronic Science and Engineering, University of Electronic Science and Technology of China, Chengdu, China. [7]School of Environmental and Chemical Engineering, Shanghai University, Shanghai, China. [8]State Key Laboratory of Mechanics and Control of Mechanical Structures, and Institute of Nanoscience, Nanjing University of Aeronautics and Astronautics, Nanjing, China. [9]CINTRA CNRS/NTU/THALES, Research Techno Plaza, Singapore, Singapore. [10]Department of Chemistry, City University of Hong Kong, Kowloon, Hong Kong, China. [11]School of Electrical and Electronic Engineering, Nanyang Technological University, Singapore, Singapore. [12]Environmental Chemistry and Materials Centre, Nanyang Environment and Water Research Institute, Singapore, Singapore. [13]These authors contributed equally: Yongmin He, Qiyuan He
*e-mail: qjwang@ntu.edu.sg; HZhang@ntu.edu.sg; hua.zhang@cityu.edu.hk; z.liu@ntu.edu.sg

Supplementary Information

Self-gating in semiconductor electrocatalysis

Yongmin He[1,2†], Qiyuan He[1†], Luqing Wang[3], Chao Zhu[1], Prafful Golani[1], Albertus D. Handoko[4], Xuechao Yu[2], Caitian Gao[2], Mengning Ding[5], Xuewen Wang[1], Fucai Liu[6], Qingsheng Zeng[1], Peng Yu[1], Shasha Guo[1], Boris Yakobson[3], Liang Wang[7], Zhi Wei Seh[4], Zhuhua Zhang[8], Minghong Wu[7], Qi Jie Wang[2, 9*], Hua Zhang[1,10*], and Zheng Liu[1,9,11,12*]

[1]School of Materials Science and Engineering, Nanyang Technological University, Singapore 639798, Singapore.

[2]Center for OptoElectronics and Biophotonics, School of Electrical and Electronic Engineering & The Photonics Institute, Nanyang Technological University, Singapore 639798, Singapore.

[3]Department of Materials Science and NanoEngineering, Rice University, Houston, Texas 77005, United States.

[4]Institute of Materials Research and Engineering, Agency for Science, Technology and Research (A*STAR), 2 Fusionopolis Way, Innovis, Singapore 138634, Singapore.

[5]Key Laboratory of Mesoscopic Chemistry of MOE, School of Chemistry and Chemical Engineering, Nanjing University, Nanjing 210023, China.

[6]School of Optoelectronic Science and Engineering, University of Electronic Science and Technology of China, Chengdu 610054, China.

[7]School of Environmental and Chemical Engineering, Shanghai University, Shanghai 200444, P.R. China.

[8]State Key Laboratory of Mechanics and Control of Mechanical Structures, and Institute of Nanoscience, Nanjing University of Aeronautics and Astronautics, Nanjing 210016, China.

[9]CINTRA CNRS/NTU/THALES, UMI 3288, Research Techno Plaza, Singapore, Singapore.

[10]Department of Chemistry, City University of Hong Kong, Kowloon, Hong Kong, China.

[11]School of Electrical and Electronic Engineering, Nanyang Technological University, Singapore, Singapore

[12]Environmental Chemistry and Materials Centre, Nanyang Environment and Water Research Institute, Singapore, Singapore.

[†]Yongmin He and Qiyuan He contributed equally to this work.

[*]E-mail: z.liu@ntu.edu.sg, HZhang@ntu.edu.sg, hua.zhang@cityu.edu.hk, and qjwang@ntu.edu.sg

Contents

1 Materials and methods

Figure S1. Four types of micro-cells fabricated in this work.

There are four types of micro-cells developed in our work, as shown in Figure S1, *i.e.*, Type 1: micro-cell for *in-situ* electronic/electrochemical measurement, which can simultaneously collect the electronic and electrochemical signals of semiconductor electrocatalysts at a large potential window; Type 2: micro-cell for thickness-dependent electrocatalytic measurement, which can examine the HER performance of MoS_2 with various thicknesses (1-101 nm) to obtain the penetration depth of the surface conductance (in this micro-cell, the electrochemical current transports vertically through the semiconductor to the bottom electrode); Type 3: micro-cell for top and bottom electrode measurement, which can investigate the surface and bulk conductance of the semiconductor flake; and Type 4: micro-cell for photoelectrochemical measurement, which can measure not only the photo-conductance and photo-electrochemical current simultaneously, but also the photo-response time at various electrochemical potentials.
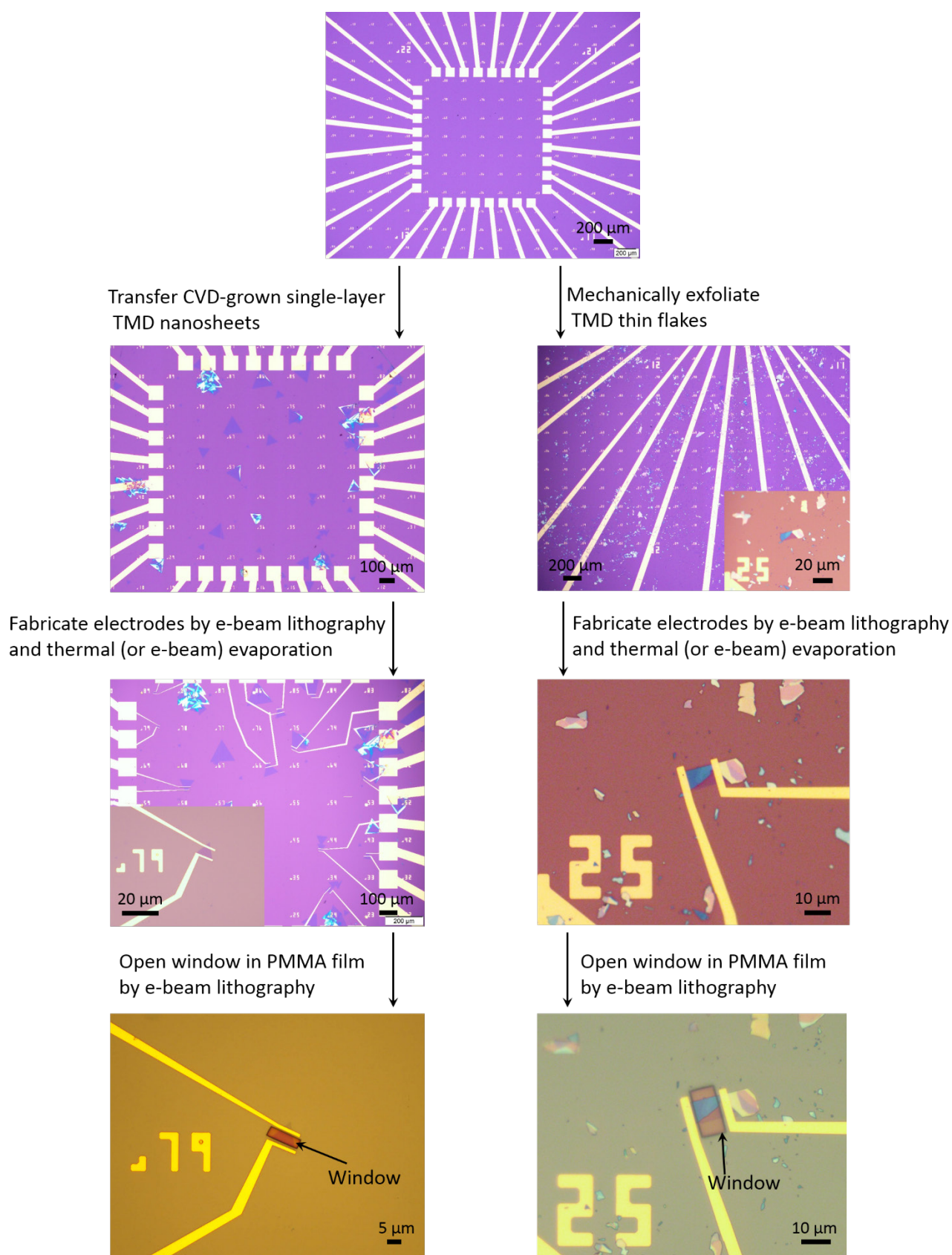
Figure S2. Device fabrication procedures for the micro-cells.

The typical fabrication procedure is shown in Figure S2. First, a 16 mm × 16 mm SiO₂ (285 nm)/Si

chip with pre-patterned 32 Au contact pads was fabricated using the conventional photolithography. Then, the CVD-grown single-layer WS_2 (left panels in Figure S2) or mechanically exfoliated TMDs (MoS_2, WSe_2, $WSe_{1.8}Te_{0.2}$,[1] $ReSe_2$, $PtSe_2$ and $MoTe_2$) nanosheets (right panels in Figure S2) were transferred onto the chips. The mechanically exfoliated TMD nanosheets were treated by the Ar plasma (3 W at 6.5×10^{-3} Torr for 15 s) to create S, Se, or Te vacancies (2-4%) to provide more active sites[2]. After that, the e-beam lithography, followed by thermal or electron-beam evaporation, were used to fabricate metal contacts used for the drain and source, which contact the Au pads on the chip (metal contacts: Cr (5 nm)/Au (60 nm) for MoS_2, ReS_2, and single-layer WS_2; Pd (5 nm)/Au (60 nm) for $WSe_{1.8}Te_{0.2}$; Ti (5 nm)/Au (60 nm) for WSe_2, $PtSe_2$, and $MoTe_2$). Finally, the device chip was passivated with 1-μm-thick poly(methylmethacrylate) (PMMA) film, followed by the e-beam lithography process to open a window through PMMA to expose the region of interest on the nanosheet.
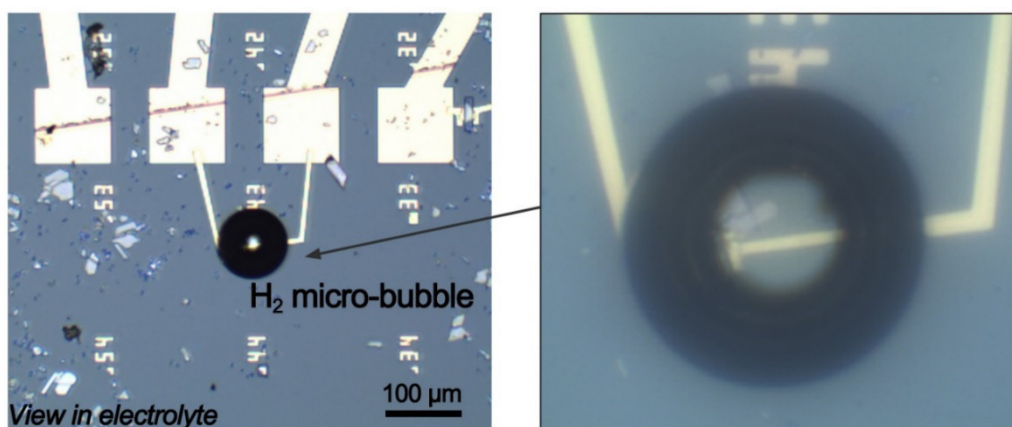
Figure S3. Identification of the electrocatalytic reaction occurred at the exposed area of MoS₂ in micro-cell.
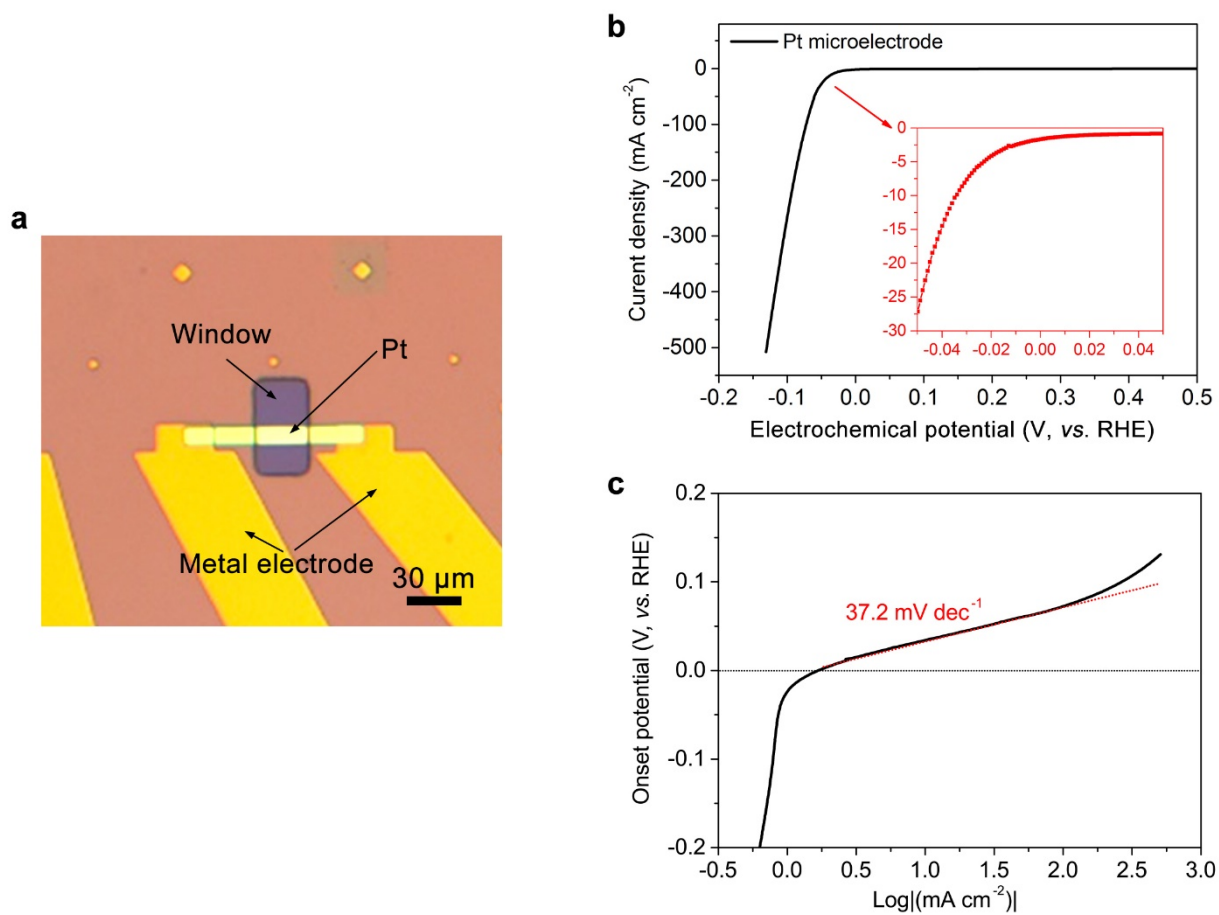
Figure S4. Calibration of the micro-cell on Pt microelectrode. (a) Optical image of Pt microelectrode with thickness of 40 nm. (b) Polarization curves of Pt microelectrode and (c) the corresponding Tafel plot.
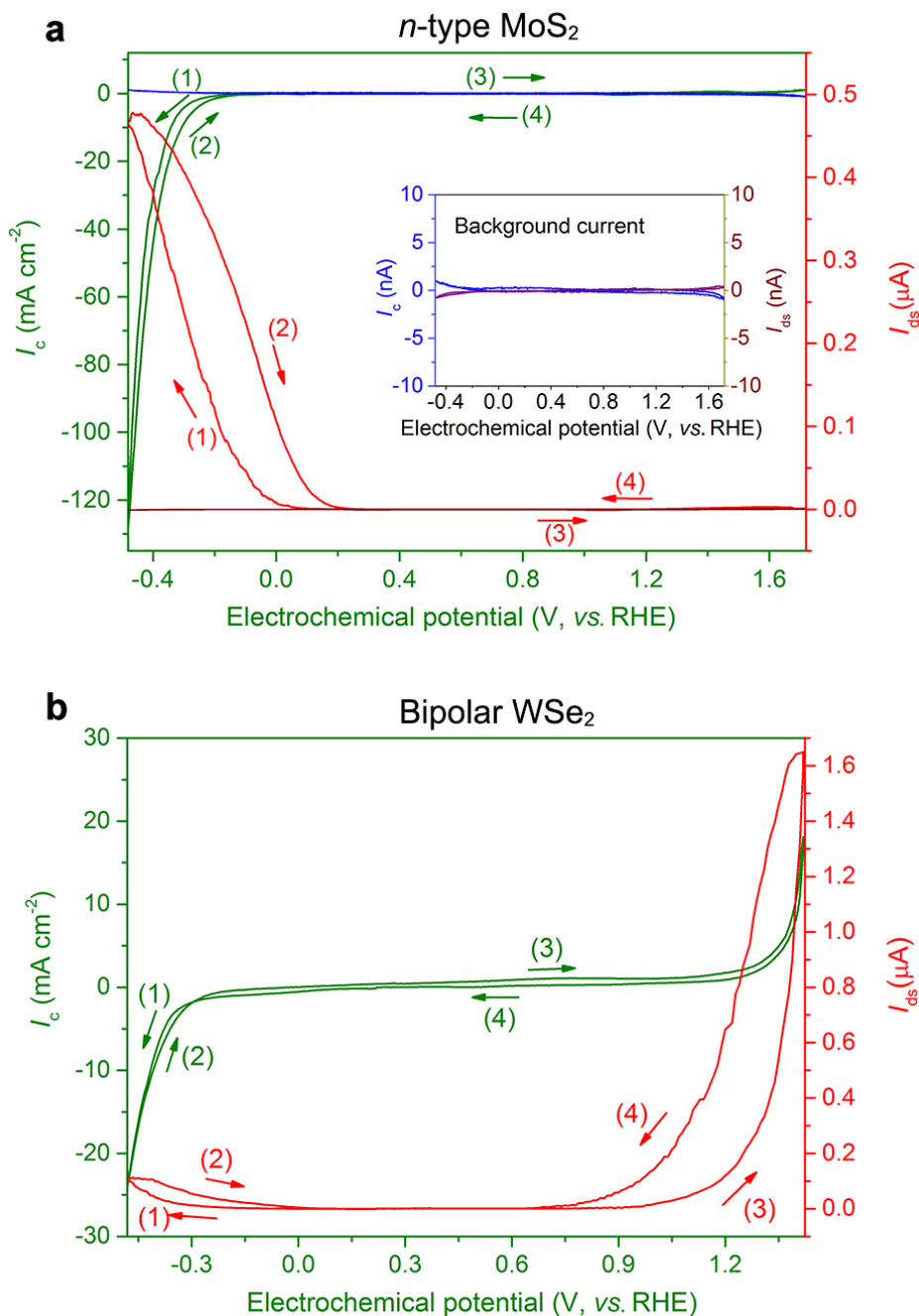
Figure S5. The typical *in-situ* electronic/electrochemical measurements in micro-cells with the electrochemical potential scanned through zero → cathodic (HER) → zero → anodic (OER) → zero (marked as (1)-(4) in the plot). The electronic signal (I_{ds}, red curve) and the electrochemical signal (I_c, green curve) were collected simultaneously on *n*-type MoS$_2$ (a) and bipolar WSe$_2$ (b) nanosheets. Inset in (a): the background currents of I_c (typically <10^{-9} A, green curve) and I_{ds} ($\approx 10^{-10}$ A, red curve), measured in micro-cell passivated with PMMA without opening window are negligible, indicating no electrochemical reaction and no conductance modulation during the measurement.

2 Electrical circuit diagram of four-electrode micro-cell

The equivalent circuit diagram used in the four-electrode micro-cell consisting two source measurement units (SMU), *i.e.*, SMU 1 (Keithley 2400) and SMU 2 (Keithley 2450), are shown in Figure S6. SMU1 is used for the electronic measurement, where the "High Force (Force HI)" and "Low Force (Force LO)" are connected to the source and drain electrodes on semiconductor catalyst, respectively. The corresponding current (I_{ds}) is collected during the electrocatalytic reaction. SMU2 is used for the three-electrode electrochemical measurement, where both "Low Force (Force LO)" and "Low Sense (Sense LO)" terminals are connected with the working electrode. The "High Force (Force HI)" and "High Sense (Sense HI)" terminals were connected to the counter electrode and reference electrode, respectively. The corresponding electrochemical current (I_c) is collected on SMU2. These two measurements are synchronized by the general purpose interface bus (GPIB) and the Labview script, allowing simultaneous recording of the electronic and the electrochemical signals.
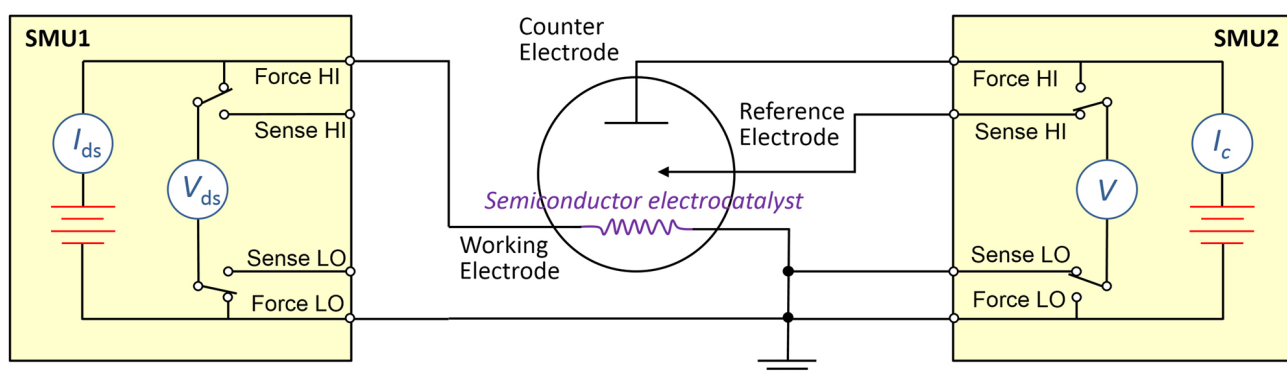
Figure S6. The equivalent circuit diagram illustrating the *in-situ* electronic/electrochemical measurement. SMU1 is used for the electronic measurement, and SMU2 is used for the three-electrode electrochemical measurement.

3 Demonstration of the self-gating

In the electronic measurement in micro-cell, I_{ds} is about 10-1000 times greater than I_c, which is dependent on the conductance of the nanosheets and the bias voltage (V_{ds}) used in the experiment. As shown in Figure S7a-b, I_c is about 20 nA while I_{ds} is about 600-700 nA at V_{ds} = 50 mV in the single-layer WS$_2$ device. In order to further prove the validity of I_{ds}, we have varied V_{ds} from 0 to 50 mv. I_{ds} clearly follows the change of V_{ds} while showing no obvious effect on I_c (Figure S7c), which is confirmed by the Tafel plots at various bias voltage (V_{ds}: 0, 5, 10, 20 and 50 mV) in the Figure S7d. In the electrochemical measurement, the single-layer WS$_2$ nanosheet shows an onset potential of $\approx$ -208 mV and Tafel slope of $\approx$ 108 mV dec^{-1} (Figure S7d), which are comparable with previously reports[3,4]. The slight difference in Tafel plots suggests that the bias potentials (0-50 mV) applied in the electronic measurement did not alter the electrochemical signals.
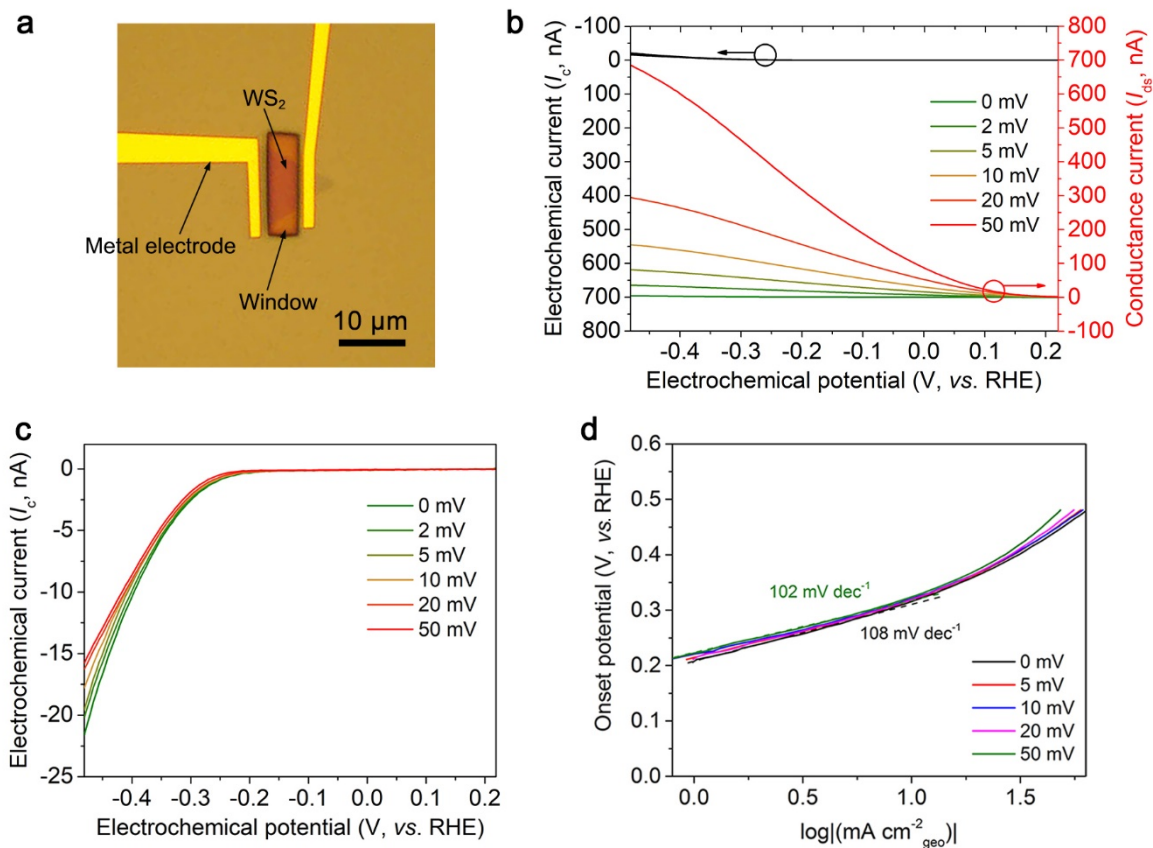
Figure S7. Electrochemical measurement on single-layer WS$_2$ nanosheet during HER. (a) Optical image of single-layer WS$_2$ micro-cell with reaction window in the PMMA film. (b) Absolute electrochemical current (y axis in black) and electronic current (y axis in red) of single-layer WS$_2$ during hydrogen evolution reaction (HER) at varied bias potentials (V_{ds}: 0, 2, 5, 10, 20 and 50 mV). (c) The zoom-in electrochemical current of black curves in (b) at varied bias potentials. (d) The corresponding Tafel plots of the single-layer WS$_2$ in HER at various bias potentials (V_{ds}: 0, 5, 10, 20 and 50 mV) obtained from Figure 1c in the main text (polarization curves, black y axis).

Supplementary Note 1: Theoretical calculation of the change of electrostatic potential ($\Delta\phi$)

The electrostatic potential in the gate modulation is given by,

$$e\Delta\phi = \frac{e^2 n}{C_G} \tag{1}$$

where n is the majority carrier concentration, e is the elementary charge, $\Delta\phi$ is the change of electrostatic potential, and C_G is the geometric capacitance of the electrolyte (0.5 M H_2SO_4 in our experiment). C_G equals to $\frac{\varepsilon_r \varepsilon_0}{d_{edl}}$, where ε_0 is the vacuum dielectric constant, ε_r is the relative dielectric constant of the solvent, and d_{edl} is the thickness of EDL. The d_{edl} approximately equals to 1.5 k^{-1},[5] in which k^{-1} is the Debye-Hückel length given by

$$k^{-1} = \sqrt{\frac{KT\varepsilon_r \varepsilon_0}{2CZ^2 e^2}} \tag{2}$$

where K is the Boltzmann constant, T is the temperature, ε_0 is the vacuum dielectric constant, ε_r is the relative dielectric constant of the solvent, C is the concentration of the electrolyte, e is the elementary charge, and Z is the charge of the ions. In 0.5 M H_2SO_4, the thicknesses of EDL under positive and negative gatings are estimated to be 0.34 and 0.45 nm, respectively. Hence, C_G is estimated to be 200 and 160 $\mu F\ cm^{-2}$ under the positive gating and the negative gating, respectively. Finally, $\Delta\phi$ is caculated to be $\phi = \frac{en}{C_G} = 9.06 \times 10^{-16} n$ under the positive gating, and $\phi = \frac{en}{C_G} = 7.25 \times 10^{-16} n$ under negative gating.

Prior to the *in-situ* electronic/electrochemical measurements in micro-cell, the back-gated measurement was first carried out. As schematic illustration in Figure S8a, the MoS_2 nanosheet (thickness of <10 nm) with Cr/Au contact (5/60 nm) shows the *n*-type characteristic (Figure S8b), the $WSe_{1.8}Te_{0.2}$ nanosheet with Pd/Au (5/60 nm) contact exhibits the *p*-type characteristic (Figure S8c), and the WSe_2 nanosheet with Ti/Au (5/60 nm) contact gives the typical bipolar characteristic (Figure S8d). Based on our experiment, the exposed areas of the *n*-type MoS_2, *p*-type $WSe_{1.8}Te_{0.2}$, and bipolar WSe_2 nanosheets are measured to be 41, 43, and 69 μm^2, respectively. The thicknesses of the *n*-type MoS_2, *p*-type $WSe_{1.8}Te_{0.2}$, and bipolar WSe_2 nanosheets are measured to be 4, 2, and 14 nm, respectively.
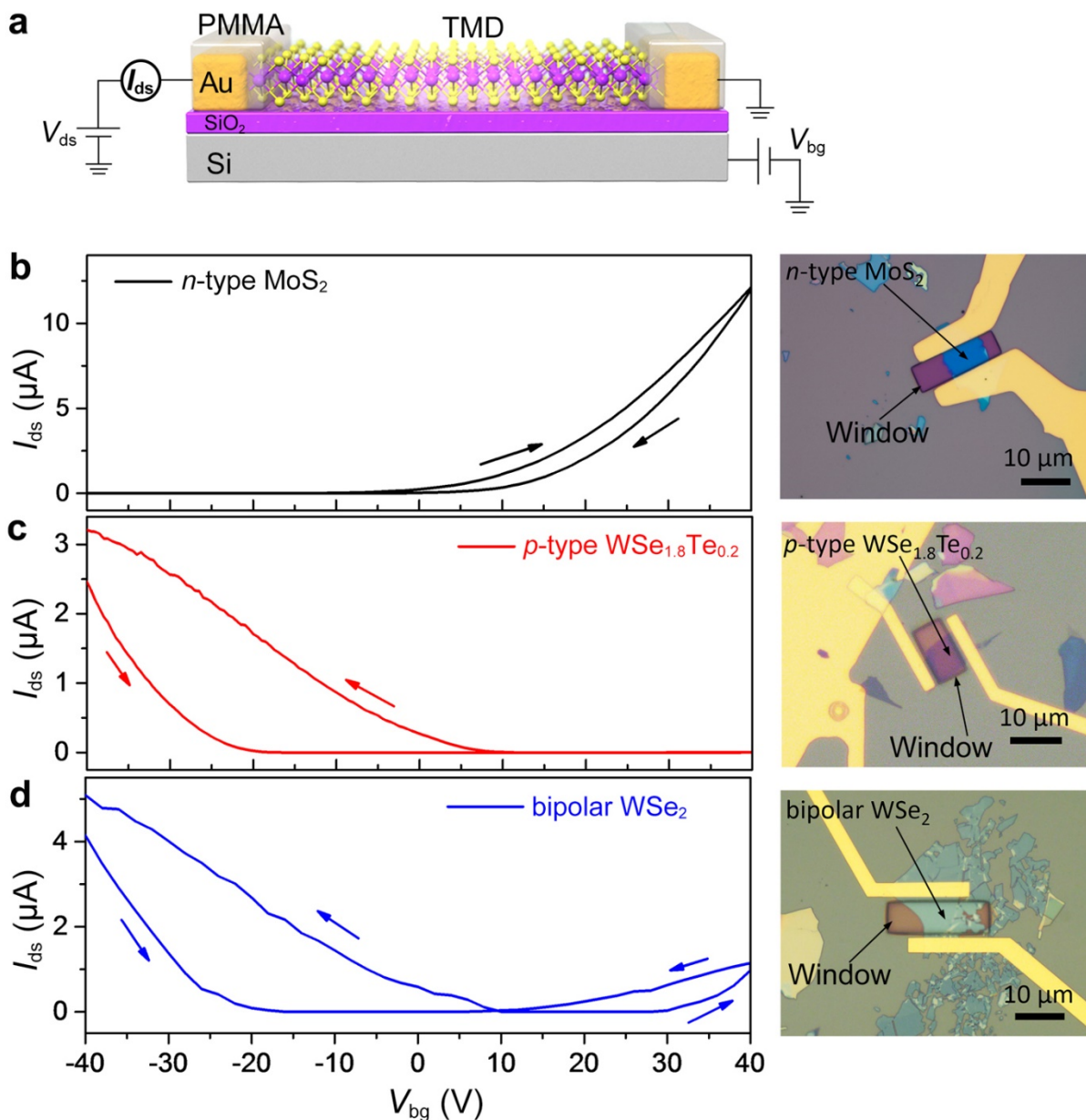
Figure S8. Back-gated measurements of TMD nanosheets on SiO₂ (285 nm)/Si substrates. (a) Schematic illustration of TMD micro-cell. (b) Transfer curves of *n*-type MoS₂ nanosheet (left panel) and the corresponding optical image of micro-cell (right panel). (c) Transfer curves of *p*-type WSe₁.₈Te₀.₂ nanosheet (left panel) and the corresponding optical image of micro-cell (right panel). (d) Transfer curves of bipolar WSe₂ nanosheet (left panel) and the corresponding optical image of micro-cell (right panel).

Supplementary Note 2. Experimental data for the effecient tuning of the Fermi level by self-gating

The bipolar WSe2 is turned on at negative and positive electrochemical potentials (top panel of Figure 1f in the main text, which is also list below), and the corresponding Fermi level is tuned close to the band edges of the conduction band and the valence band, respectively. When applying the equation $\Delta V_{\mathrm{G}} = \Delta E_{\mathrm{f}}/e + \Delta\phi$ to the ΔV_{G} interval (OFF-state: ΔV_{GAP}), we can get:

$$e\Delta V_{\mathrm{GAP}} = e(\Delta V_{th}^{e} - \Delta V_{th}^{n}) = \Delta E_{\mathrm{f}} \tag{3}$$

where ΔE_{f} is the bandgap, ΔV_{th}^{e} is the threshold voltage of electrons, ΔV_{th}^{n} is the threshold voltage of holes, and e is the elementary charge. According to the equation (3), the bandgap of WSe2, *i.e.*, $\Delta E_{\mathrm{f}}(\mathrm{WSe}_2) \approx 1.13$ eV, can be exacted from the self-gating characteristics in Figure 1f shown below.
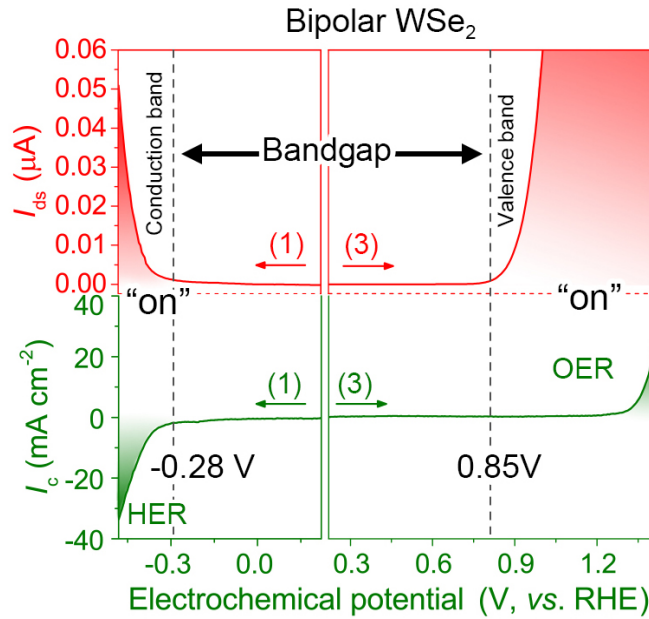
Figure 1f. *In-situ* electronic/electrochemical measurements of bipolar WSe2. The red curves in top panels are obtained from the electronic measurements, and the green curves in bottom panels are obtained from the electrochemical measurements. The bipolar WSe2 is turned on both negative and positive electrochemical potentials, and then delivers the HER and OER, respectively. Accordingly, its Fermi level is tuned to the band edges of the conduction band and the valence band, respectively, experimentally identifying the bandgap.
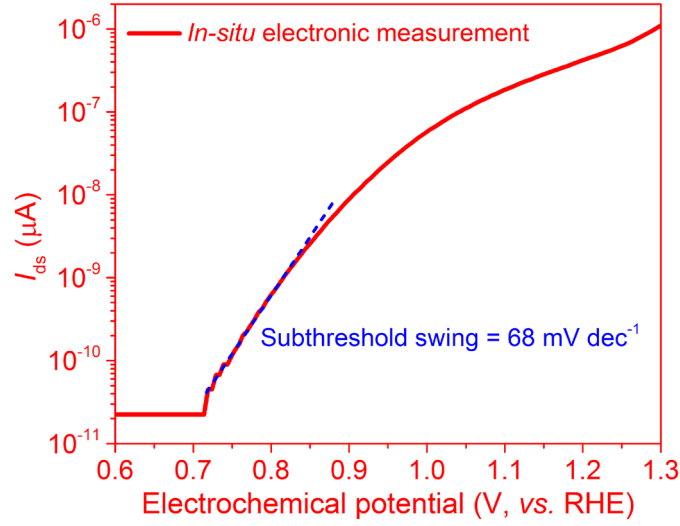
Figure S9. Transfer curve of bipolar WSe₂ nanosheet at the positive electrochemical potential under self-gating from the *in-situ* electronic measurement in the top panel in Figure 1f. It shows a subthreshold swing of 68 mV dec⁻¹ for holes under positive gating.

The subthreshold swing (*SS*) is given by

$$SS = ln(10)\frac{KT}{e}(1 + \frac{C_S}{C_G})$$ (4)

where *e* is the electron charge, C_S is the capacitance of semiconductor (as for the ultrathin semiconductor, it is considered as the quantum capacitance, *i.e.*, C_q), and C_G is the geometric capacitance. C_G is much greater than C_q when the ultrathin semiconductor is at the off state, resulting in an ideal *SS* of 60 mV dec⁻¹ at room temperature.

From the *in-situ* electronic measurement in Figure 1f, the *SS* for the electron accumulation of bipolar WSe₂ under the positive electrochemical potential can be extracted from the transfer curve based on the following equation,

$$SS = \frac{\partial V_g}{\partial (log_{10}I)}$$ (5)

where V_g is the electrochemical potential in self-gating, and *I* is the I_{ds} current. As shown in Figure S9, the *SS* is calculated to be 68 mV dec⁻¹, which is close to the ideal value (60 mV dec⁻¹), further confirming a highly efficient modulation of the Fermi level by self-gating during the electrocatalysis.

ReS₂ electrocatalyst: Figure S10a shows the Raman spectrum of ReS$_2$ nanosheet, which is consistent with reported work[6]. The optical image of the ReS$_2$ micro-cell is shown in the inset of Figure S10a. Figure S10c shows the *in-situ* electronic/electrochemical measurement in the ReS$_2$ micro-cell. In the electronic measurement, ReS$_2$ shows an *n*-type characteristic with an on/off ratio of 5×10^3 under self-gating during the electrocatalytic reaction (Figure S10c, red curve), agreeing with the back-gated measurement on the same device on SiO$_2$ (285 nm)/Si substrate (Figure S10b) and recently reported work.[6] In the electrochemical measurement, *n*-type ReS$_2$ is turned on by the negative potential, while it is turned off by the positive potential under self-gating, only exhibiting the HER activity (Figure S10c, black curve). Its corresponding Tafel plot is shown in Figure S10d, showing an onset potential of $\approx$ -156 mV (*vs*. RHE) and Tafel slope of $\approx$ 122 mV dec^{-1}.

Figure S10. Self-gating on ReS₂ nanosheet. (a) Raman spectrum of ReS$_2$ nanosheet. Inset: optical image of the ReS$_2$ micro-cell with reaction window in the PMMA passivated film. (b) Back-gated measurement of the ReS$_2$ nanosheet, showing an *n*-type semiconducting behavior. (c) *In-situ* electronic/electrochemical measurement of ReS$_2$ nanosheet, in which the red curve shows the electronic signal and the black curve shows the electrochemical signal. (d) The corresponding Tafel plot of the ReS$_2$ nanosheet in HER.

PtSe₂ electrocatalyst: Figure S11a shows the Raman spectrum of PtSe$_2$ nanosheet , which is consistent with reported work[7]. The optical image of the PtSe$_2$ micro-cell is shown in the inset of Figure S11a. Figure S11c shows the *in-situ* electronic/electrochemical measurement of the PtSe$_2$ micro-cell. In the electronic measurement, PtSe$_2$ delivers a bipolar characteristic under self-gating (Figure S11c, red curve), which is also confirmed by the back-gated measurement on the same device (Figure S11b). In the electrochemical measurement, PtSe$_2$ can be turned on by both the negative and positive potentials, showing a remarkable HER activity (Figure S11c, black curve). Its corresponding Tafel plot gives an onset potential of ≈ -100 mV (*vs*. RHE) and Tafel slope of ≈ 106 mV dec^{-1} (Figure S11d).

In our experiment, dozens of PtSe$_2$ devices have been tested. They can be turned on at both positive and negative electrochemical potentials. However, only HER activity was observed, and no ORE activity happened. These results confirm that the high conductance is not the only factor to determine the electrocatalytic activity. This indicates that the conductance of the semiconductor catalyst ("on" and "off") is necessary for the electrocatalysis to happen. A high conductance does not guarantee a high catalytic performance, because the "intrinsic catalytic activity" of the semiconductor is another important factor[8], which is related to the adsorption/desorption kinetics (charge transfer) of the reactants on the catalyst surface. In the other word, the self-gating makes the charge transport from electrode to the surface of semiconductor, while the "intrinsic catalytic activity" dominates the charge transfer process at the interface. Both of them contribute to the semiconductor electrocatalysis.
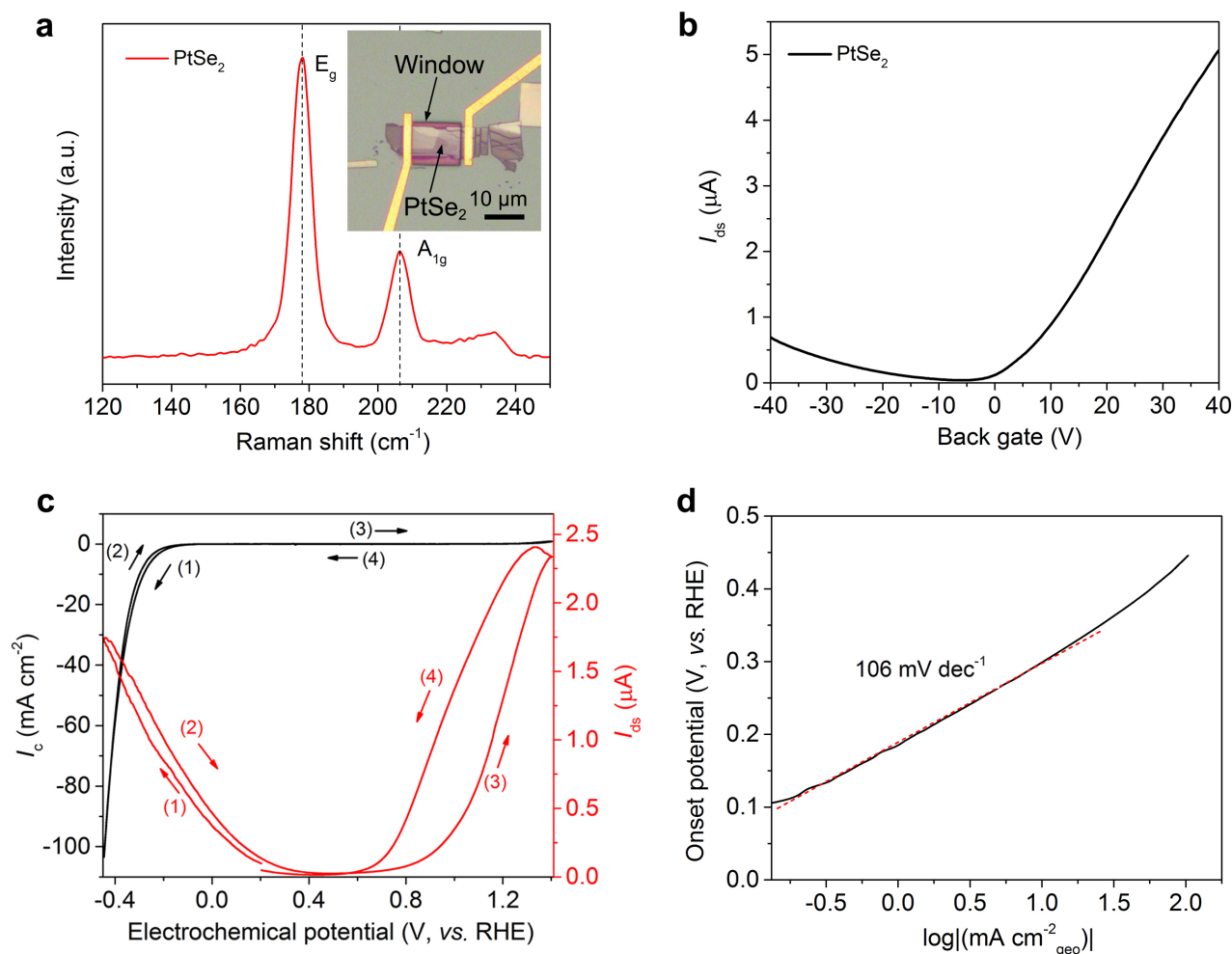
Figure S11. Self-gating on PtSe₂ nanosheet. (a) Raman spectrum of PtSe₂ nanosheet. Inset: optical image of PtSe₂ micro-cell with reaction window in the PMMA passivated film. (b) Back-gated measurement of PtSe₂ nanosheet on the SiO₂ (285 nm)/Si substrate, showing a bipolar characteristic. (c) *In-situ* electronic/electrochemical measurement of PtSe₂ nanosheet, in which the red curve shows the electronic signal and the black curve shows the electrochemical signal. (d) The corresponding Tafel plot of the PtSe₂ nanosheet in HER.

MoTe₂ electrocatalyst: Figure S12a shows the Raman spectrum of MoTe$_2$ nanosheet with 2H phase, which is consistent with reported work[9]. The optical image of the MoTe$_2$ micro-cell is shown in the inset of Figure S12a. Figure S12c shows the *in-situ* electronic/electrochemical measurement of the MoTe$_2$ micro-cell. In the electronic measurement, 2H MoTe$_2$ shows an *n*-type semiconducting characteristic with an on/off ratio 6×10^3 under self-gating (Figure S12c, red curve), which was further confirmed by back-gated measurement on the same device (Figure S12b). In the electrochemical measurement, the 2H MoTe$_2$ is turned on by the negative potential during the electrocatalytic reaction, and thus shows the HER activity (Figure S12c, black curve). Its corresponding Tafel plot gives an onset potential of $\approx$ -256 mV (*vs*. RHE) and Tafel slope of $\approx$ 86 mV dec^{-1} (Figure S12d).
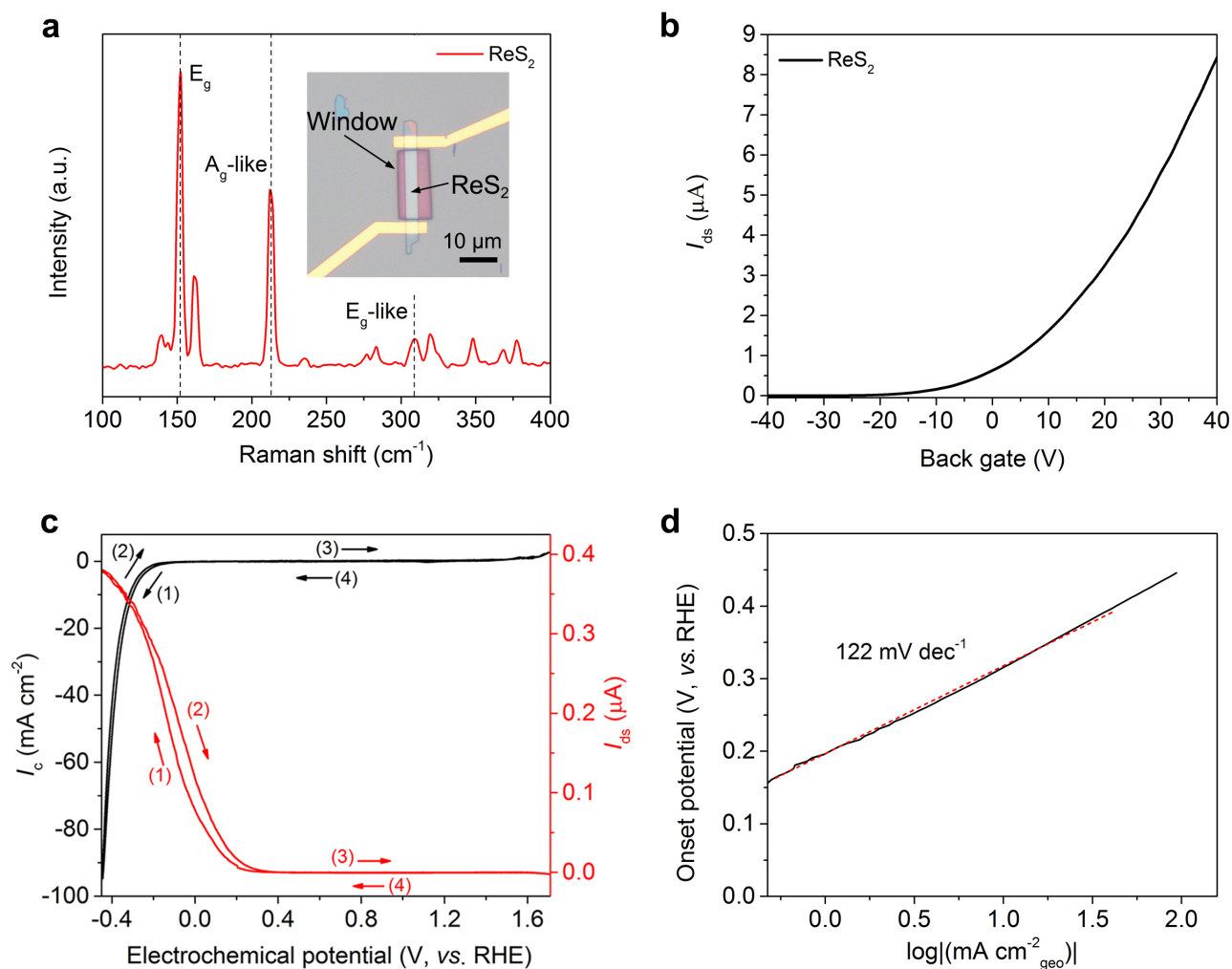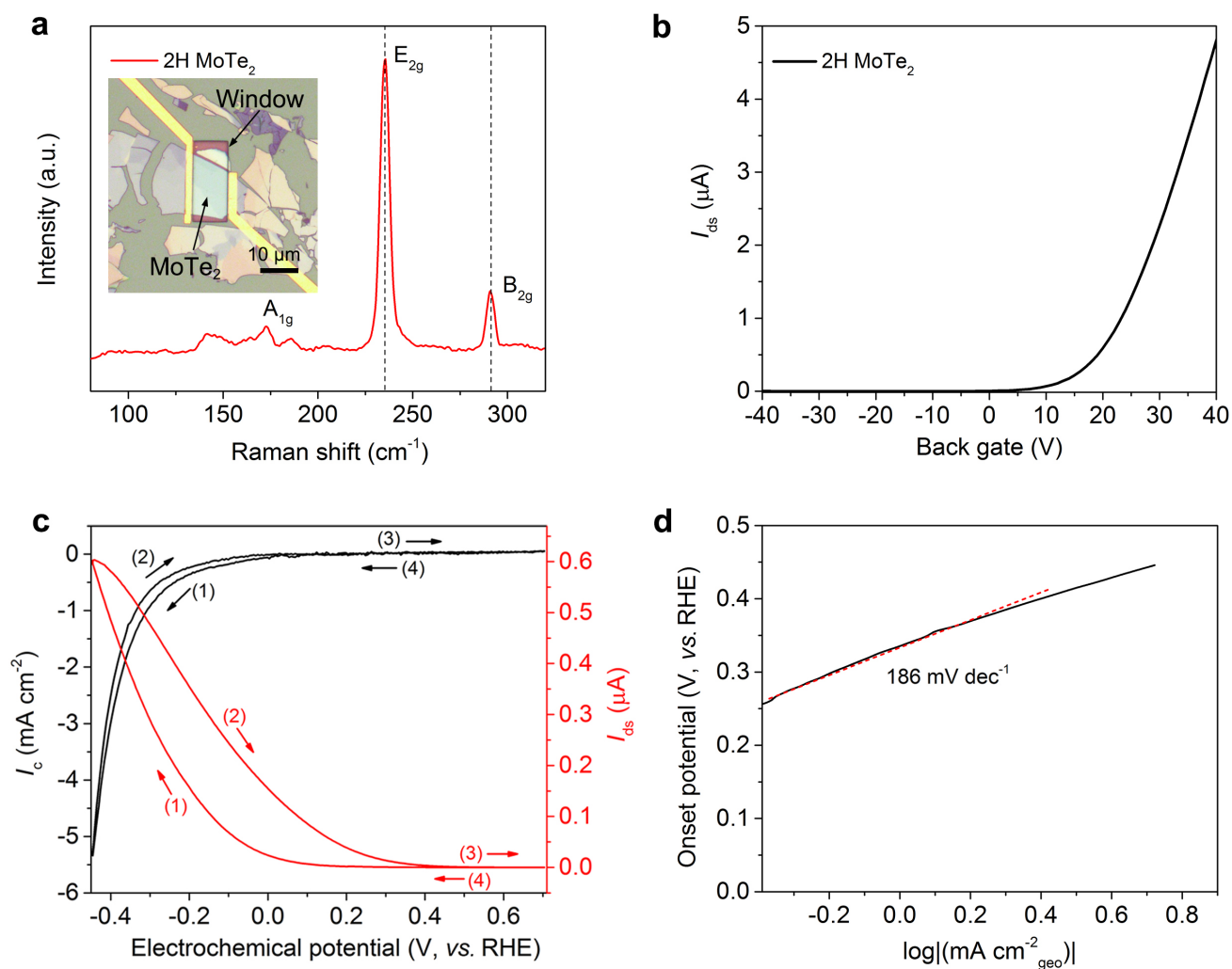
Figure S12. Self-gating on 2H MoTe₂ nanosheet. (a) Raman spectrum of 2H MoTe₂ nanosheet. Inset: optical image of 2H MoTe₂ device with reaction window in the PMMA passivated film. (b) Back-gated measurement of 2H MoTe₂ nanosheet on the SiO₂ (285 nm)/Si substrate, showing an *n*-type characteristic. (c) *In-situ* electronic/electrochemical measurement of 2H MoTe₂ nanosheet, in which the red curve shows the electronic measurement and the black curve shows electrochemical measurement. (d) The corresponding Tafel plot of the 2H MoTe₂ nanosheet in HER.

We first introduced different KCl into 0.5 M H_2SO_4 electrolyte to investigate the effect of salt ions on the electrocatalytic reaction and self-gating. As shown in Figure S13a-c, a significant decrease of electrochemical current without obvious change of I_{ds} was observed, indicating the self-gating is stable. Furthermore, we did the self-gating experiments in pure KCl solution, PBS buffer, and phosphate buffer, showing similar phenomenon with very small electrochemical current (Figure S13e-g).
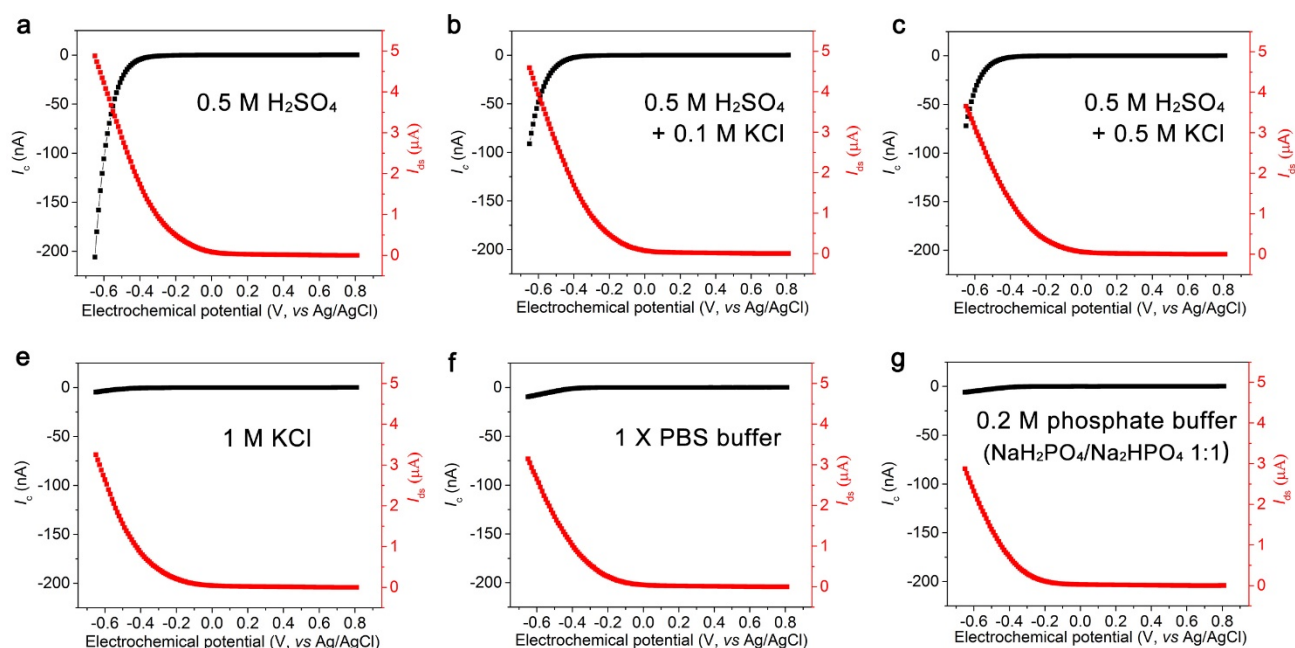
Figure S13 Self-gating in different types of solutions. *In-situ* electronic/electrochemical measurement of a MoS_2 device in 0.5 M H_2SO_4 solution (a), mixed H_2SO_4/KCl solutions: 0.5 M H_2SO_4/0.1 M KCl solution in (b) and 0.5 M H_2SO_4/0.5 M KCl solution in (c), 1 M KCl solution (e), PBS buffer (f), and phosphate buffer (g).

The *n*-type MoS$_2$ only shows HER activity with an onset potential of $\approx$ -165 mV (*vs*. RHE) and Tafel slope of $\approx$ 116 mV dec^{-1} (Figures 1d and Figure S14a). These values are comparable to recently reported values of CVD-grown MoS$_2$[2,10-13]. The *p*-type WSe$_{1.8}$Te$_{0.2}$ only shows OER activity with an onset potential of $\approx$ 1.31 V (*vs*. RHE) and Tafel slope of $\approx$ 118 mV dec^{-1} (Figures 1e and Figure S14b). The bipolar WSe$_2$ shows both HER activity (Figures 1f and Figure S14c, onset potential of $\approx$ -295 mV *vs*. RHE and Tafel slope of $\approx$ 128 mV dec^{-1}) and OER activity (Figures 1f and Figure S14d, onset potential of $\approx$ 1.33V *vs*. RHE and Tafel slope of $\approx$ 101 mV dec^{-1}). It is worth mentioning that the OER performances of *p*-type WSe$_{1.8}$Te$_{0.2}$ and bipolar WSe$_2$ in our experiment are comparable to recently reported values of the N and P co-doped porous carbon used as an electrocatalyst[14].
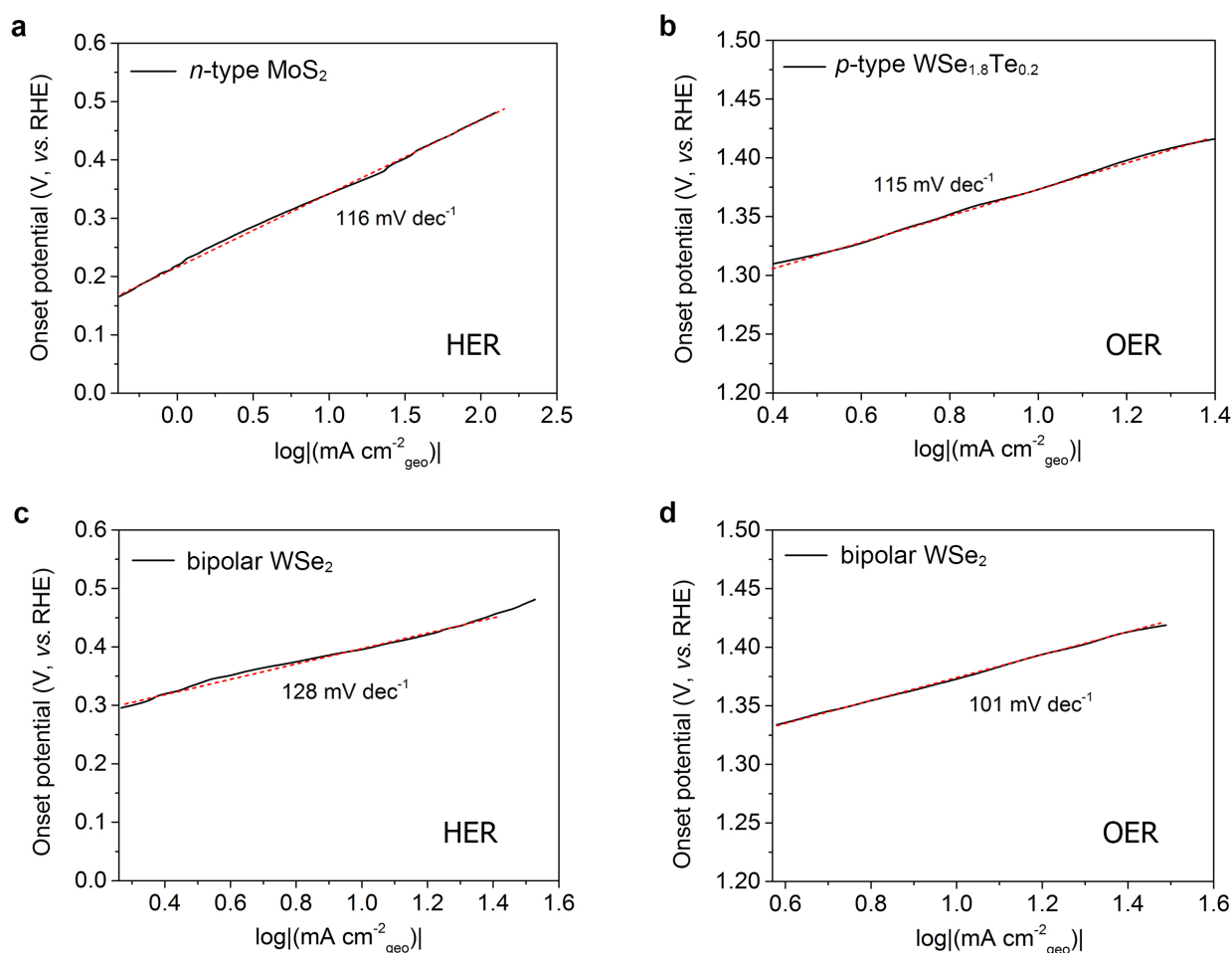
Figure S14. The corresponding Tafel plots of *n*-type MoS$_2$ (a), *p*-type WSe$_{1.8}$Te$_{0.2}$ (b), and bipolar WSe$_2$ (c-d) in Figures 1d-f in the main text.

4 Identification of the self-gating by the electrochemical impedance spectroscopy measurement in micro-cell

A modified transmission line (TL) model[15] is used to explain the electrochemical impedance spectroscopy (EIS) measurement (Figure S15) and compare the results from *in-situ* electronic/electrochemical measurement. The TL model is often considered in the EIS analysis when the intermediate charge transport cannot be neglected in conducting polymers and porous film electrodes. As shown in the bottom panel in Figure S15, a TL model on a 1D line electrode is used by repeating the unit of charge transport process (r_{ctt} and r_q) in series with faradic charge transfer process (r_{ctr} and q_{edl}), in which

$$r_{ctt} = R_{ctt}/L \tag{6}$$

$$c_q = C_q/L \tag{7}$$

$$r_{ctr} = R_{ctr}/L \tag{8}$$

$$q_{edl} = Q_{edl}/L \tag{9}$$

where R_{ctt} is the charge transport resistance of the line electrode, r_{ctt} is the charge transport resistance per unit length, R_{ctr} is the charge transfer resistance of the line electrode, r_{ctr} is the charge transfer resistance per unit length, C_q is the quantum capacitance of the line electrode, c_q is the quantum capacitance per unit length, Q_{edl} is the constant phase element of the line electrode, q_{edl} is the constant phase element per unit length, and L is the length of the 1D line electrode. It is worth mentioning that the TL model is based on the assumption of homogenous distribution of the position-independent elements along the 1D line electrode. This assumption can simplify the equivalent circuit in order to interpret the experimental data. We exclude the contribution of both the electrical circuit and the solution resistance (R_s) because they are several orders of magnitude

smaller than the charge transport resistance (R_{ctt}) and the charge transfer resistance (R_{ctr}). As shown in Figure S15, the measurements between the terminals A and B, and terminals A and C represent the electronic and electrochemical measurements, respectively. Therefore, the equivalent charge transport resistance (R_{ctt}) calculated from the *in-situ* electronic measurement can be expressed by:

$$R_{ctt} = \frac{\sum_{x=0}^{L} x\frac{R}{L}}{L+1} = \frac{R}{2} \tag{10}$$

where R is the total resistance of the electrode obtained from the *in-situ* electronic measurement, in which $R = dV_{ds}/dI_{ds}$.
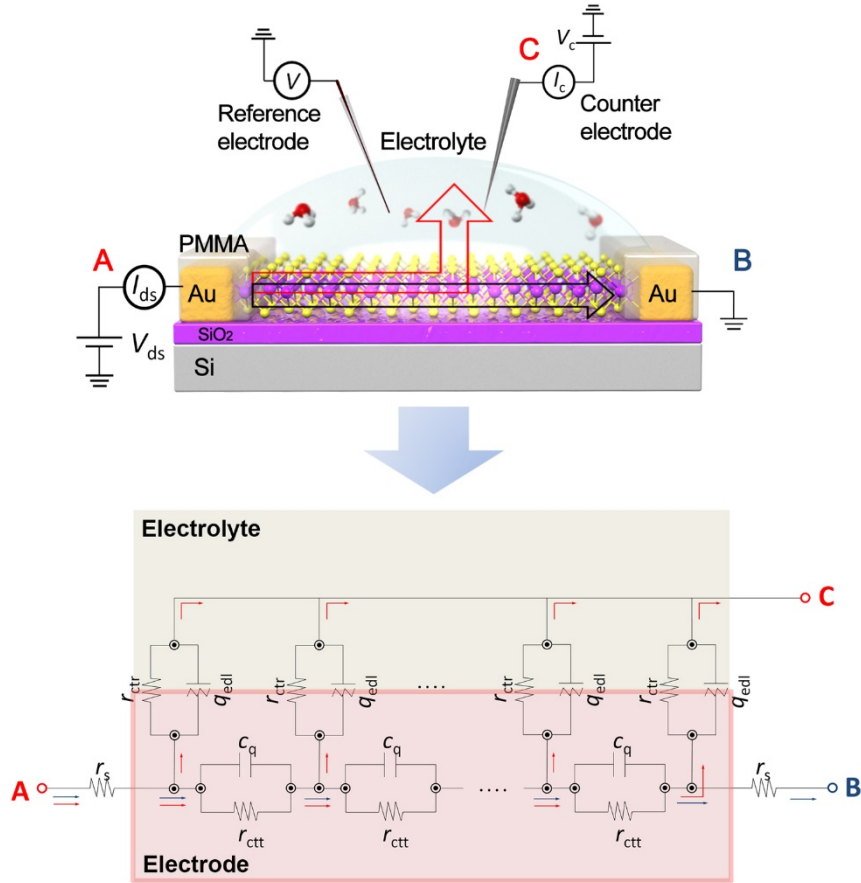
Figure S15. Equivalent circuit based on the transmission line (TL) model to compare the *in-situ* electronic measurement on terminals (A-B) and the EIS measurement on terminals (A-C). Top: Schematic illustration of *in-situ* electronic/electrochemical measurement; Bottom: Equivalent circuit of *in-situ* electronic/electrochemical measurement in micro-cell.

Au microelectrode: Figure S16a shows the optical image of Au microelectrode. Figure S16b gives its HER performance with an onset potential of $\approx$ -154 mV (*vs*. RHE), Tafel slope of $\approx$ 114 mV dec^{-1}, and current density of about 100 mA cm^{-2} at 0.4 V (*vs*. RHE) The Tafel slope of Au microelectrode is comparable to that of the mechanical exfoliated MoS$_2$ (Figure S14a), suggesting a similar charge transfer process at the HER electrocatalytic interface. Figure S16c-e show the R_{ctr}, C_{edl}, and Bode magnitude (|Z|) of Au microelectrode at various HER potentials from the EIS measurement, respectively. The Au microelectrode delivers a C_{edl} of about 300-400 μF cm^{-2} during the HER process (Figure S16d). It is worth mentioning that the slight fluctuation of C_{edl} at the HER potentials (-0.16 to -0.36 V, *vs*. RHE), indicates the quasi-stable nature of the EDL with minimal interference from the charge transfer process in electrocatalytic reaction.
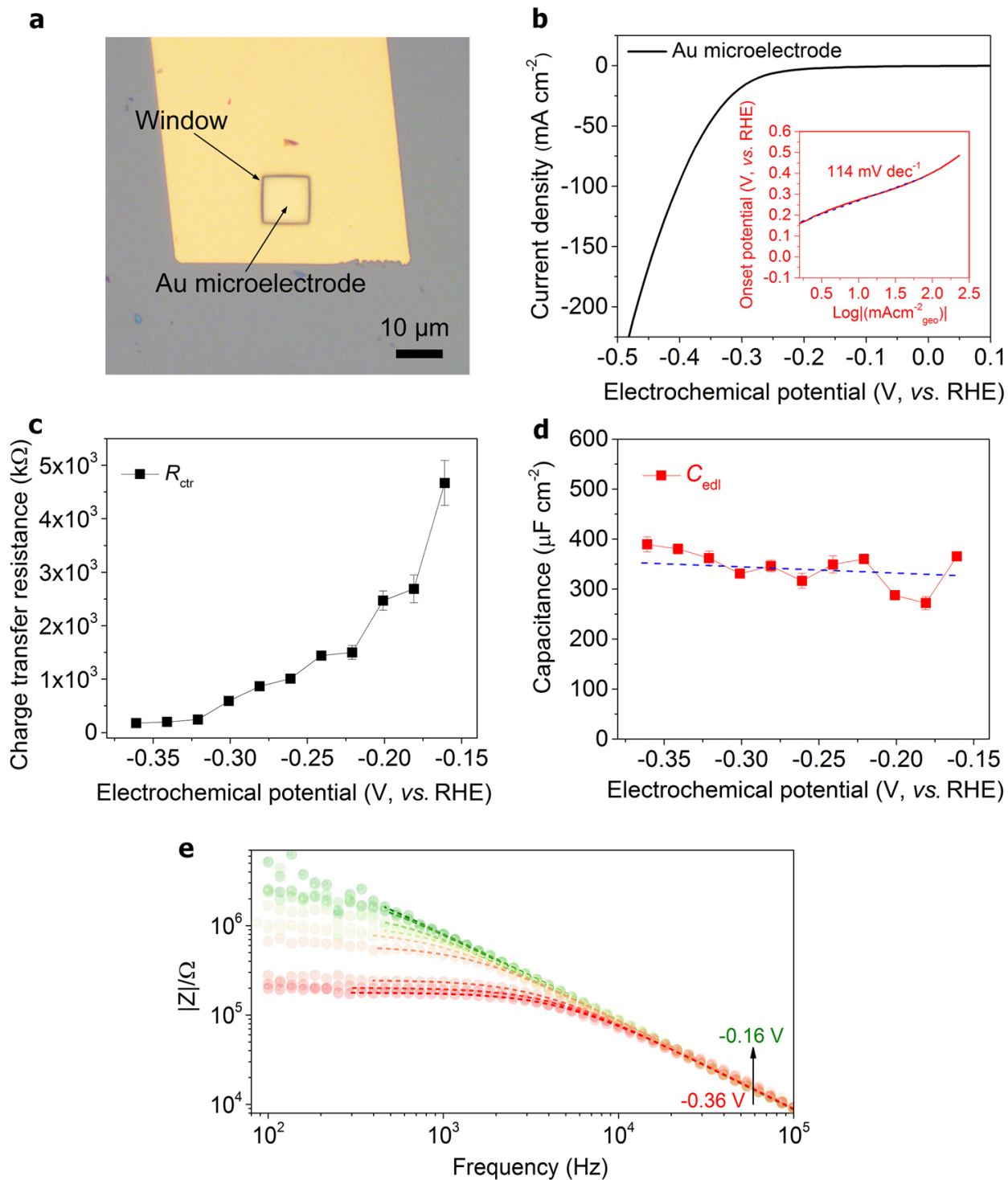
Figure S16. HER and EIS measurements of Au microelectrode in the micro-cell. (a) Optical image of Au microelectrode with an open window of 100 μm². (b) The polarization curve of Au microelectrode. Inset: the corresponding Tafel plot. (c)-(d) Variations of R_{ctr} (c) and C_{edl} (d) of Au microelectrode collected from the fitting data of the equivalent circuit at various HER potentials in Table S1. (e) Representative Bode magnitude (|Z|) of Au microelectrode at various HER potentials from 100 kHz to 100 Hz with an amplitude of 10 mV.

For Au microelectrode, Q_{edl} is related to the EDL capacitance at the metal-electrolyte interface, and R_{ctr} is the charge transfer resistance.

In Table S1, C_{edl} can be obtained from the Hsu and Mansfeld's equation[16,17],

$$C = Q^{\frac{1}{N}} \times R^{\frac{1-N}{N}} \tag{11}$$

where Q is a constant phase element, and R is parallel resistance from the equivalent circuit. When N = 1, Q behaves as a pure capacitor. When N = -1, Q behaves as a pure inductance. In addition, we observed that the internal resistance (R_s) in micro-cell is significantly smaller (from 10 to several-hundred Ω) comparable to R_{ctr} (from 10 kΩ to several MΩ) in Au microelectrode. Similarly, R_s is also much smaller than R_{ctt} and R_{ctr} in MoS$_2$ nanosheet microelectrode, which will be discussed later. Therefore, R_s is ignored in our experiment. It is worth mentioning that such ultra-small R_s has been also frequently observed in the high impedance measurement of the corrosion electrochemical behavior in the paint coating systems by EIS[18,19].

Table S1. The optimum fitting parameters of equivalent Randles circuit elements (R_s + Q_{edl}/R_{ctr}) with one time constant (CPE_{edl}) for Au microelectrode measured at the various HER potentials from 100 kHz to 100 Hz with an amplitude of 10 mV.

η	R_{ctr}	Q_{edl}	N_{edl}	X^2	C_{edl}
(V, *vs*. RHE)	(kΩ)	(pMho*s^N)		(fitting deviation)	(μF cm^{-2})
-0.16	4670	234	0.979	0.0118	365.6761
-0.18	2690	213	0.988	0.0117	272.1157
-0.20	2470	212	0.985	0.0106	287.8147
-0.22	1500	241	0.98	0.0113	360.3067
-0.24	1440	234	0.98	0.0097	349.3398
-0.26	1010	214	0.98	0.0116	316.5996
-0.28	867	239	0.981	0.0095	346.3141
-0.30	591	226	0.98	0.0101	331.0846
-0.32	246	242	0.978	0.0118	361.9991
-0.34	202	246	0.976	0.0101	380.3541
-0.36	179	248	0.975	0.0098	389.526

Abbreviations: η: the electrochemical overpotential; R_{ctr}: the charge transport resistance; Q_{edl}: the constant phase element related to the electrical double layer capacitance at the metal-electrolyte interface; X^2: the fitting deviation; C_{edl}: the electrical double layer capacitance.

MoS₂ nanosheet microelectrode: Figure S17a-b show the optical image and the *in-situ* electronic/electrochemical measurement of the MoS₂ nanosheet, respectively. Figure S17c-e show R_{ctr}, C_{edl}, and Bode magnitude $|Z|$) of MoS₂ nanosheet microelectrode at various HER potentials from the EIS measurement, respectively. The C_{edl} of MoS₂ nanosheet microelectrode (Figure S17d) is comparable to that of Au microelectrode, indicating similar Faradic charge transfer process and EDL characteristic during HER. A quasi-stable C_{total} of 50-60 μF cm^{-2} in HER is obtained for the MoS₂ nanosheet microelectrode (Figure S17d), indicating a stable self-gating with minimal influence from the electrocatalytic reaction.

It is worth mentioning that C_{total} of MoS₂ in our EIS measurement is greater than those reported in MoS₂-based electric double-layer transistors (EDLTs)[20-23], such as MoS₂/ion-gel interfaces (*e.g.*, 5.78 μF cm^{-2} at 15 Hz[22] and 10.7 μF cm^{-2} at 0.1 Hz[20]). This difference could be attributed to the following three factors: **(i)** Aqueous electrolyte. C_{edl} is much greater in the aqueous electrolyte due to a larger dielectric constant of water as compared to the ion-gel electrolyte. **(ii)** Greater C_q. In our work, EIS measurements are conducted at electrochemical potentials from -0.131 to -0.381 V (*vs*. RHE), in which MoS₂ is turned on with Fermi level inside the conduction band. This is different from the reported measurements of EDLTs which are typically conducted at the gate voltage close to 0 V, *i.e.*, MoS₂ is at the off state. As a result, those measurements of MoS₂-based EDLTs[20-23] lead to a much smaller C_q, because the Fermi level is located in the bandgap. As a contrast, in our EIS measurements, the Fermi level is already turned inside the conduction band, resulting in a much greater C_q. **(iii)** Different measurement systems. There are usually extra interface capacitors involved in the reported measurements of EDLTs, leading to an inaccurate estimation of the total specific capacitance. For example, the applied two-electrode system without the reference electrode contains an extra solid-

liquid interface on the counter electrode, and the exposed drain and source metal electrodes without passivation contain extra metal-liquid interfaces. However, we are able to exclude these extra interface capacitors by using a reference electrode and the selective exposure of MoS_2 nanosheet to the electrolyte (with the PMMA passivation).
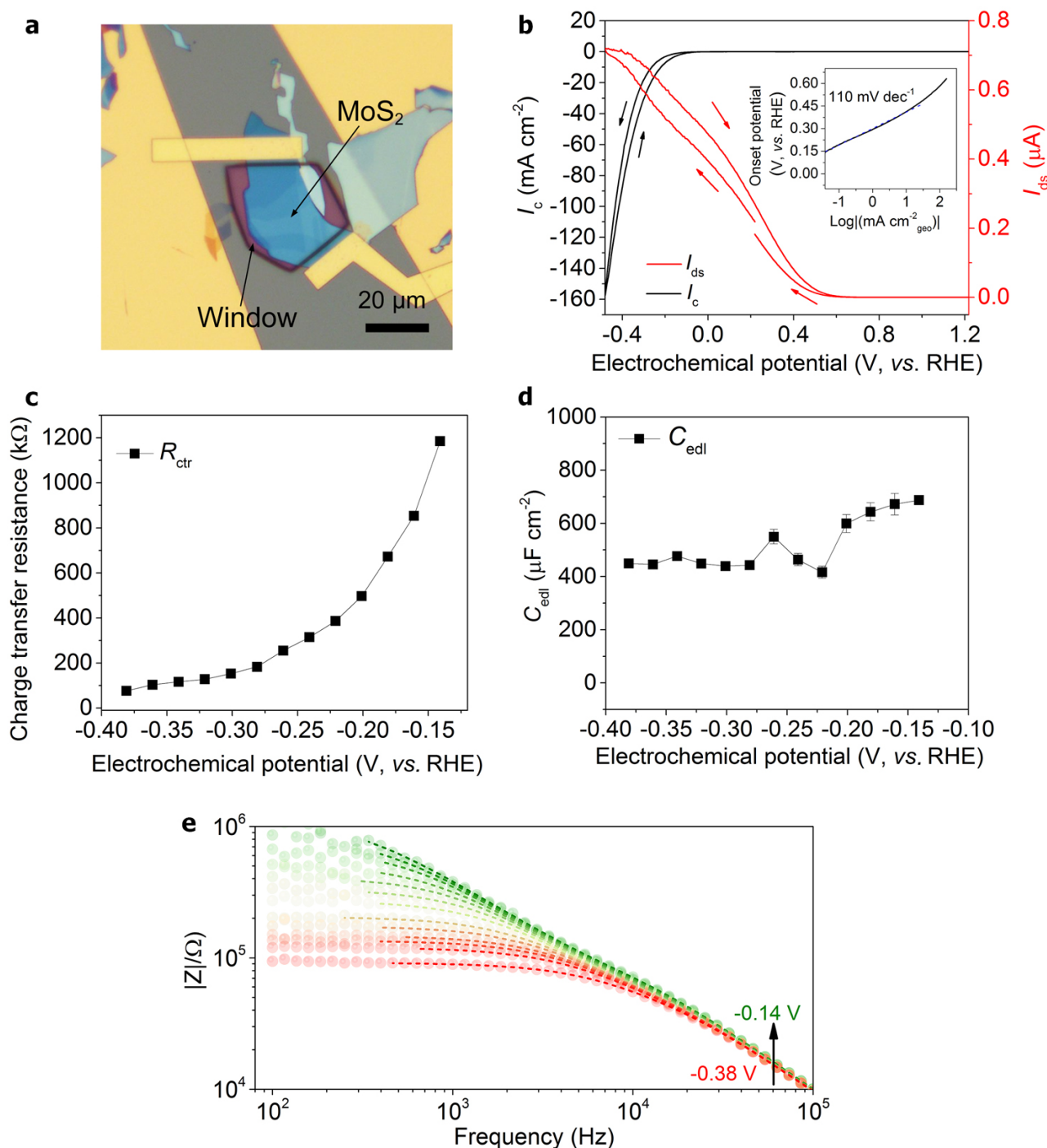
Figure S17. EIS and *in-situ* electronic/electrochemical measurements of MoS₂ nanosheet microelectrode. (a) Optical image of 8-nm-thick MoS₂ nanosheet microelectrode with an open window of 650 μm². (b) The *in-situ* electronic/electrochemical measurement of 8-nm-thick MoS₂ nanosheet microelectrode in (a). Inset: the corresponding Tafel plot showing an onset potential of ≈ -146 mV, Tafel slope of ≈ 110 mV dec⁻¹, and current density of about 88 mA cm⁻² at 0.4 V (*vs.* RHE). (c)-(d): R_{ctr} (c) and C_{edl} (d) of MoS₂ nanosheet microelectrode collected from the fitting data of the equivalent circuit at various HER potentials in Table S2. (e) Representative Bode magnitude (|Z|) of MoS₂ nanosheet microelectrode at various HER potentials from 100 kHz to 100 Hz with an amplitude of 10 mV.

As shown in Table S2, the time constant ($R_{ctr}Q_{edl}$) is associated with the charge transfer at the MoS$_2$-electrolyte electrocatalytic interface (the faradic process), and the additional time constant ($R_{ctt}Q_q$) is associated with the charge transport in MoS$_2$ nanosheet microelectrode, as compared to Au microelectrode. Specifically, both R_{ctt} and Q_q are strongly dependent on the electrochemical potentials due to the self-gating.

It is worth mentioning that in a conventional electrochemical cell, similar equivalent Randles circuit ($Q_1/R_1+Q_{edl}/R_{ctr}$) with two time constants have been observed in semiconductor electrocatalysis[17,24-29], in which the Q_{edl}/R_{ctr} at low frequency is attributed to the faradic process (the charge transfer process) in the reaction and the Q_1/R_1 at high frequency corresponds to the electronic capacitance and resistivity of the film electrode[17]. However, the Q_1/R_1 is often considered potential-independent.[17,24-29] This is because the measurement of R_1 would be not accurate in the conventional electrochemical cell[17,25] due to many factors, such as extra electrocatalytic interfaces rising from the exposed conductive substrate (current collector) to electrolyte, the conductive additive (graphene or carbon black) in the electrode, or the contact between the conductive substrate and the catalysts.[27,29] However, in our micro-cell, all electrodes are effectively passivated by the PMMA, and only MoS$_2$ nanosheet is exposed for the HER test. Therefore, our EIS measurement can clearly identify the charge transport resistance and the quantum capacitance.

Table S2. The optimum fitting parameters of equivalent Randles circuit elements ($R_s+Q_q/R_{ctt}+Q_{edl}/R_{ctr}$) with two time constants (CPE_q and CPE_{edl}) for MoS$_2$ nanosheet microelectrode measured at various HER potentials from 100 kHz to 100 Hz with an amplitude of 10 mV.

η (V, *vs*. RHE)	R_{ctt} (kΩ)	R_{ctr} (kΩ)	Q_{edl} (pMho*s^N)	N_{edl}	Q_q (pMho*s^N)	N_q	X^2 (fitting deviation)	C_{edl} (μF cm^{-2})
0.14	34.6	1180	833	0.925	379	1	0.0116	686.83980
0.16	34.3	840	784	0.922	369	1	0.0062	672.11624
0.18	32.5	665	783	0.923	371	1	0.0047	642.71337
0.20	29.5	494	767	0.924	377	1	0.0042	599.06611
0.22	29.2	385	731	0.937	368	1	0.0117	416.01138
0.24	25.4	312	724	0.931	373	1	0.0027	463.40897
0.26	23.5	252	761	0.925	384	1	0.0105	549.60222
0.28	24.6	182	720	0.931	371	1	0.0101	442.62021
0.30	23.3	152	709	0.93	393	1	0.0012	438.86291
0.32	21.6	128	704	0.928	404	1	0.0013	448.58083
0.34	20.4	116	707	0.925	418	1	0.0014	476.61948
0.36	17	104	710	0.928	474	1	0.0008	445.46737
0.38	16	77.3	717	0.927	477	1	0.0010	449.17091

Abbreviations: η: the electrochemical overpotential, R_{ctt}: the charge transfer resistance; R_{ctr}: the charge transport resistance; Q_{edl}: the constant phase element related to the electrical double layer capacitance at the semiconductor-electrolyte interface; Q_q: the constant phase element related to the quantum capacitance of the semiconductor; X^2: the fitting deviation; C_{edl}: the electrical double layer capacitance.
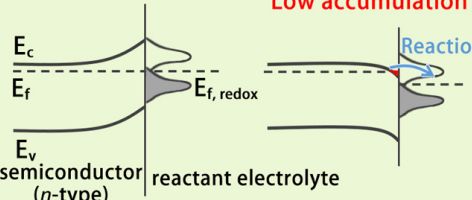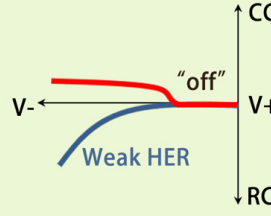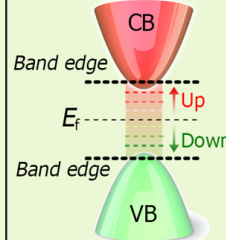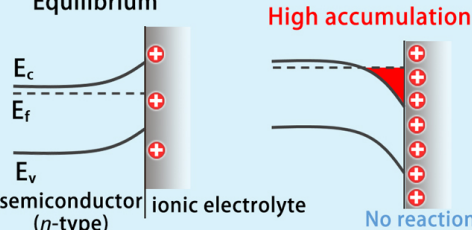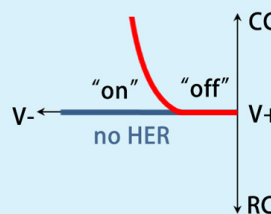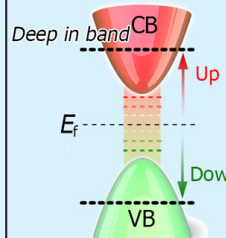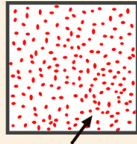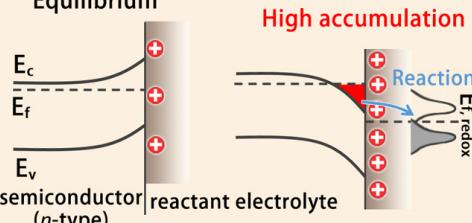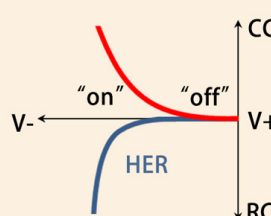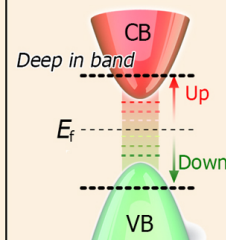
5 Carrier modulation differences between self-gating and current electron transfer theories at the semiconductor-electrolyte interface

Table S3 shows the comparison of the carrier modulation in the electron transfer theories, ion-controlled electronics (MIS junction), and the self-gating (LMIS junction). In detail, we compare the semiconductor surface, energy band structures at equilibrium and accumulation, reaction current/conductance current, and the Fermi level tuning.

Current electron transfer theories including Marcus theory and the Gerischer Model [30-35], assume a fully active semiconductor-electrolyte interface with 100% active region that works as a Schottky-analog junction[36,37]. Similar to the junction field-effect transistors[38,39], it will be difficult for such junction to accumulate a high carrier concentration or achieve a high conductivity *i.e.*, the Fermi level deep inside the conduction or valence band, as shown in Table S3 (the first row). On the other hand, the recently developed ion-controlled electronics assume a fully inert interface, which works as a ionic gating or metal-insulator-semiconductor (MIS)[37,40] (Table S3, the second row). Such gating is capable of accumulating an extremely high charge concentration (exceeding 10^{14} e cm^{-2} in 2D semiconductors) to make semiconductor conductive, or even superconductive[41,42], which is widely studied in iontronics.[43]

Based on our hundreds of devices for different types of semiconductors, we propose that, in terms of the carrier modulation, **a practical semiconductor-electrolyte interface containing both active and inert regions can be modeled as LMIS junction** (Table S3, the third row**)**. In this proposed model, **the leakage** refers to the charge transfer process at active regions (the electron transfer theories, Schottky-analog junction), and the **MIS** refers to the self-gating at the inert regions that dominates the carrier modulation, *i.e.*, a semiconductor is turned "on" or "off".

Table S3. Comparison of the carrier modulation in the electron transfer theories, ion-controlled electronics (MIS junction), and our self-gating. The semiconductor surface, energy band structures at equilibrium and accumulation, reaction current (RC)/conductance current (CC), and the Fermi level tuning, are compared.

Theory	Model	Semiconductor surface	Energy band structure	Reaction current (RC) /Conductance current (CC)	Fermi level tuning	Reference
Classic electron-transfer theories	Schottky-analog junction					[30-35]
Ion-controlled electronics	MIS junction (ionic gating)					[37, 40-43]
Self-gating	leakage MIS junction					This work

Note: Semiconductor-electrolyte interface is modeled as an analog of Schottky junction in classic electron transfer theories, referred as Schottky-analog junction in this work.

Supplementary Note 3. Comparison of Schottky-analog junction and LMIS junction

1. **Observation of a strong photo-gating during HER process**

The photogenerated excitons (electron–hole pairs) are very sensitive to the electrostatic field, because such electrostatic field can easily trap electrons or holes, and thus significantly affect the photoresponse. Here, we design a photoelectrochemical micro-cell to investigate the photoresponse of semiconductor catalysts during the HER process. Both the photo-conductance and photo-electrochemical currents can be simultaneously measured in this micro-cell. Figure S18a shows the photoelectrochemical micro-cell setup (top) and the device (bottom). A 532-nm green laser with an intensity 200 ± 2 mW cm^{-2} is used as an excitation source. ReS$_2$, a direct band-gap TMD material, is used as a semiconductor catalyst (the device performance is shown in Figure S10).

Figure S18b shows the *in-situ* electronic/electrochemical measurement of ReS$_2$ in dark (black curves) and illumination (red curves). First, a conduction modulation with an on/off ratio over 10^3 was observed in ReS$_2$ in dark, agreeing with the self-gating phenomenon (black curve in Figure S18b). Second, an enhanced photoconductivity of ReS$_2$ under light illumination was also observed (red curve in Figure S18b). Figure S18c (black curve) shows the photocurrent I_{ph}, which is defined as the difference between the conductance current under light and dark conditions, given by[44,45]:

$$I_{\mathrm{ph}} = I_{D,illum} - I_{D,dark} \tag{12}$$

where $I_{D,illum}$ is the conduction current of ReS$_2$ under light illumination, and $I_{D,dark}$ is the conduction current of ReS$_2$ in dark. Two possible mechanisms can give rise to the enhanced photoconductivity[46,47]. One is the traditional photoconductive effect, *i.e.*, once semiconductor absorbs the photons with energy larger than the bandgap (1.5 eV), electron–hole pairs will be

generated, which can be separated by the applied bias voltage and thus a photocurrent is generated. The other mechanism is the **photo-gating effect**, which rises from the defects, surface states or the electrostatic field that *traps* the photogenerated holes or electrons. It can be described as the change of threshold voltage in the dark and under light illumination, *i.e.*, ΔV_T. As a result of threshold shift, I_{ph} from the photo-gating effect can also be expressed as[44-46]:

$$I_{ph} = \frac{\partial I_D}{\partial V_g} . \Delta V_T = g_m . \Delta V_T \tag{13}$$

where g_m is the transconductance, and ΔV_T is the gate voltage (*i.e.*, the electrochemical potential in this work). As shown in Figure S18c (the right axis), an increasing g_m with the electrochemical potentials (ΔV_g) was observed before reaching the saturation region, suggesting a photo-gating effect at the semiconductor-electrolyte interface. This photo-gating effect originates from **the electrostatic field** across the semiconductor-electrolyte interface during HER process, which can trap photo-generated hole. Note that the photoconductive effect is not dependent on the gate voltage (ΔV_g)[46].

Importantly, we further observed **an enhanced photo-gating with the electrochemical potential** during HER process in our experiments, which is supported by the following experimental results, *i.e.*, **(i) the I_{ph} in the Tafel liner region** increasing with the negative electrochemical potential (the inset of Figure S18c), showing an increasing photoresponse during the HER process, and **(ii) the response time prolonged with** the electrochemical potential, as shown in Figure S18d and e (see the rising time in Figure S18e). Both (i) and (ii) indicate **an increasing electrostatic field** across the semiconductor-electrolyte interface during HER process, and such electrostatic field increases the trap time constant and the photocurrent, leading to a strong photo-gating.

The observed **enhanced photo-gating fits our LMIS model**, which **predicts an increasing electrostatic field** across the semiconductor-electrolyte interface as the charge transfer process happens. The local electrostatic field is proportional to the electrochemical potential (or V_g), and it results in **an enhanced photo-gating** during HER process. **On the contrary**, **a Schottky-analog junction model predicts a decreasing electrostatic field** across the semiconductor-electrolyte interface because the Schottky-analog junction approaches Ohmic characteristic once the charge transfer process starts. The decreasing electrostatic field leads to **a weak photo-gating** during HER process, which is similar to metal-semiconductor field-effect transistors at saturation region.[48,49]

Based on the aforementioned discussion, it is believed that the enhanced photo-gating provides **a strong evidence for LMIS junction** at the semiconductor-electrolyte interface.
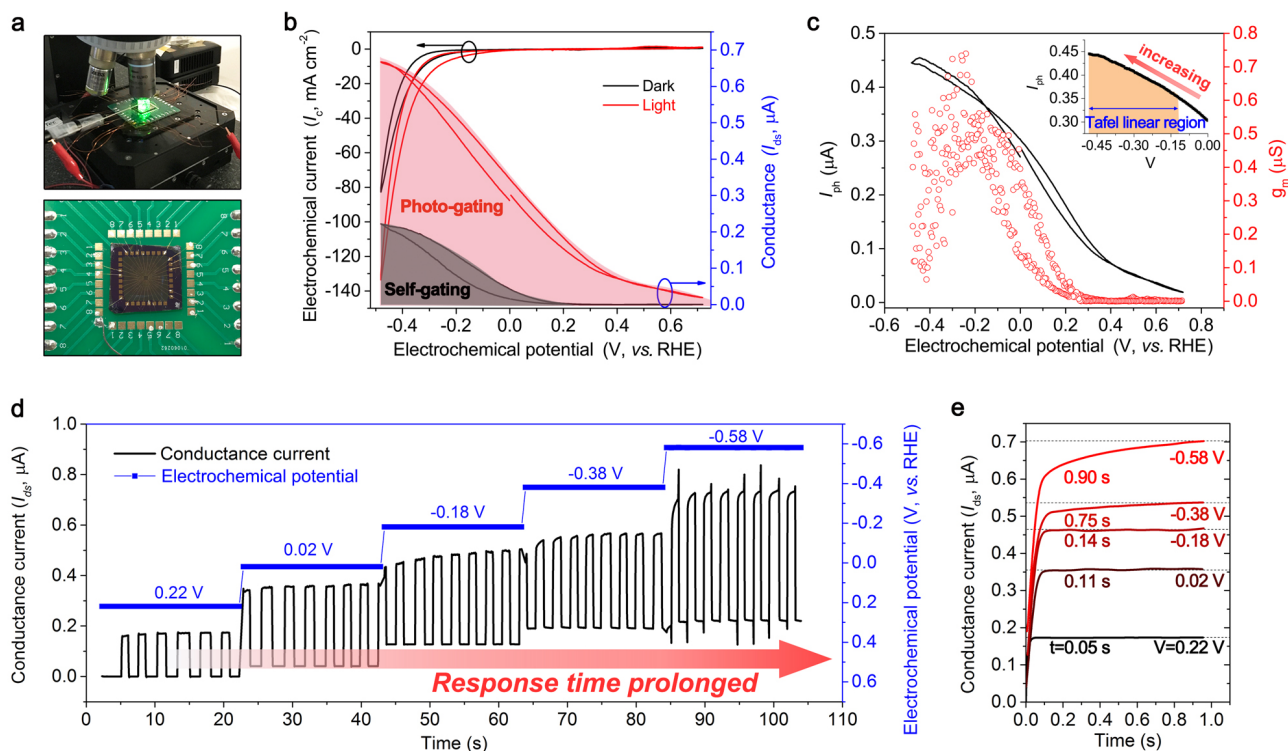
Figure S18. Strong photo-gating on ReS₂ nanosheet in photoelectrochemical micro-cell. (a) Digital images of the photoelectrochemical micro-cell setup (top) and the device (bottom). (b) *In-situ* electronic/electrochemical measurement of ReS₂ nanosheet in dark (black curve) and under illumination (red curves). (c) Electrochemical potential-dependent photogenerated current (I_{ph}, left y axis) and transconductance (g_m, right y axis) of ReS₂ nanosheet. Inset: I_{ph} at the Tafel liner region (the HER process). (d)-(e) Time-resolved photoresponse in 30 cycles (d) and 1 rising cycle (e) at different electrochemical potentials.

2. The position of Fermi level during electrocatalytic reaction:

Our *in-situ* electronic/electrochemical measurement can identify the Fermi level position of conduction or/and valence band across all potential windows. The difference between the conductance onset potential ($V_{conduct-onset}$, the edge of conduction or valence band) and the reaction onset potential ($V_{react-onset}$) is given by:

$$\Delta V = |V_{conduct-onset} - V_{react-onset}| \tag{14}$$

As shown in Figure S19, $V_{conduct-onset}$ is usually 0.3-0.7 V smaller than $V_{react-onset}$, indicating that the Fermi level is already deep inside conduction or valence bands as the HER or OER start. The Fermi level further moves deeper into conduction or valence band, as these electrocatalytic reactions continue.

Unfortunately, such deep state of the Fermi level cannot be explained by the Schottky-analog junction in the electron transfer theories. This is because the Schottky-analog junction could be broken (Ohmic characteristic) once the Fermi level is tuned into the bands. As a result, it cannot be further tuned deep in bands (see the book of "Semiconductor Physics and Devices Fourth edition" by Donald A. Neamen[37]). On the other hand, the surface of semiconductor catalyst is not considered to be fully active for charge transfer process. Instead, it should be **considered as a mixture of active and inert regions, and the carrier modulation (conductance) mainly happens at the inert regions**. In term of the carrier accumulation, our proposed LMIS junction can explain the high conductivity (the Fermi level deep in band) of semiconductors during the electrocatalysis.
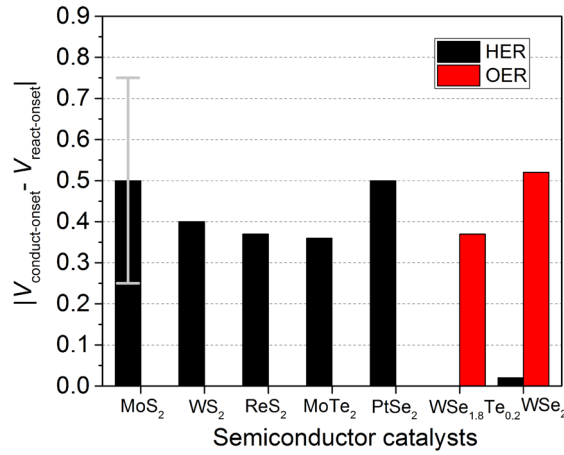
Figure S19. The potential difference between the conductance onset potential ($V_{\text{conduct-onset}}$) and the reaction onset potential ($V_{\text{react-onset}}$) of various TMD semiconductor catalysts.

3. Carrier accumulation:

As the electrocatalytic reaction starts, the accumulated carrier concentration ($n_{react-onset}$) of TMD semiconductor catalysts is given by:

$$n_{react-onset} = n_{edge\ of\ band} + \Delta n \tag{15}$$

$$\Delta n = C_{\text{total}} \times \Delta V \tag{16}$$

where $n_{edge\ of\ band}$ is the carrier concentration at the edge of conduction or valence band whose value is roughly expected to be $\approx 10^{13}$ e cm^{-2} obtained in 2D TMD-based transistors[23,40], ΔV is the potential difference between the conductance onset potential ($V_{conduct-onset}$, the edge of conduction or valence band) and the reaction onset potential ($V_{react-onset}$), C_{total} is the total capacitance of the TMD semiconductors with a range of 50-70 µF cm^{-2} which can be extracted from the EIS measurement (Figure 2i).

In our experiment, Δn of $1-3 \times 10^{14}$ e cm^{-2} can be achieved (Figure S20) when the Fermi level is tuned from the band edge to the reaction onset potentials. Therefore, an order of 10^{14} e cm^{-2} of the

carrier concentration is accumulated during HER process. As comparison, it is impossible to obtain

this value from Schottky-analog junction[49].
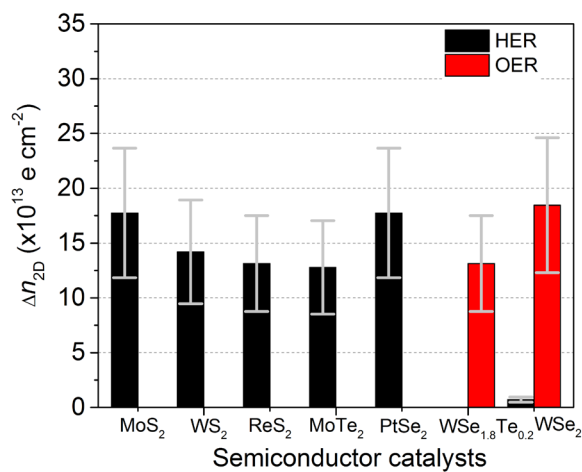
Figure S20. The carrier concentration *(△n)* accumulated from the conductance onset potential to the reaction onset potential.

6 Surface conductance of semiconductor catalysts
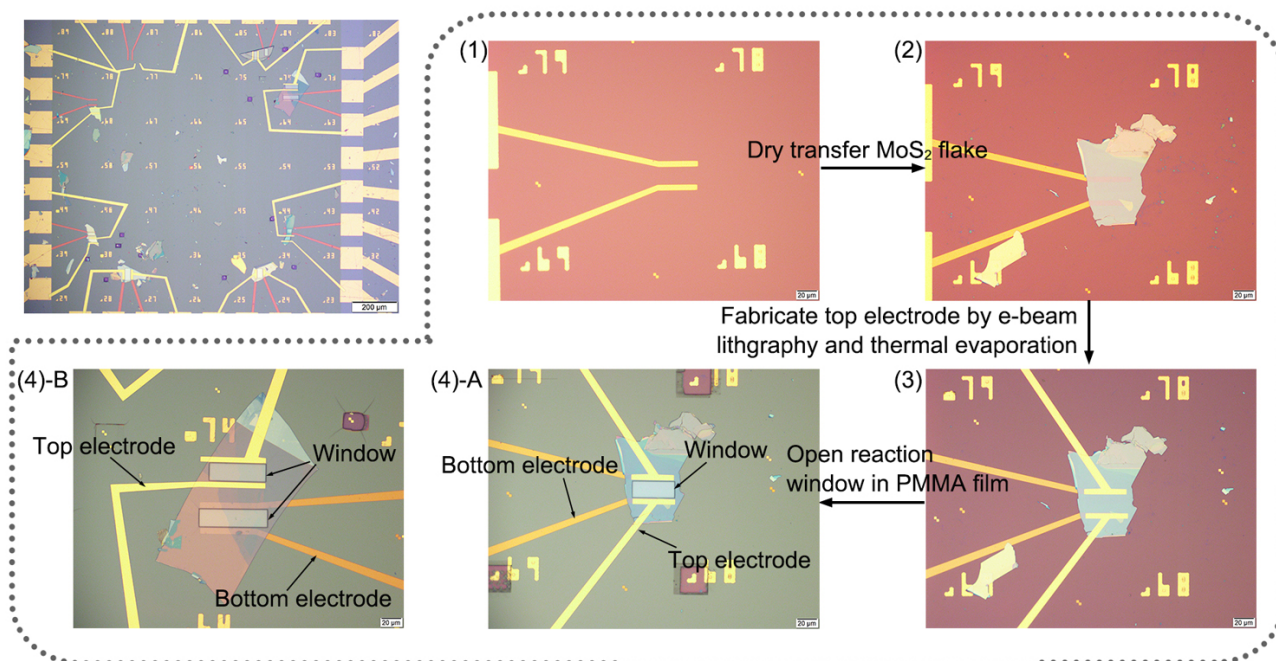
Figure S21. The fabrication procedure of MoS₂ flake-based micro-cell with top and bottom electrodes.
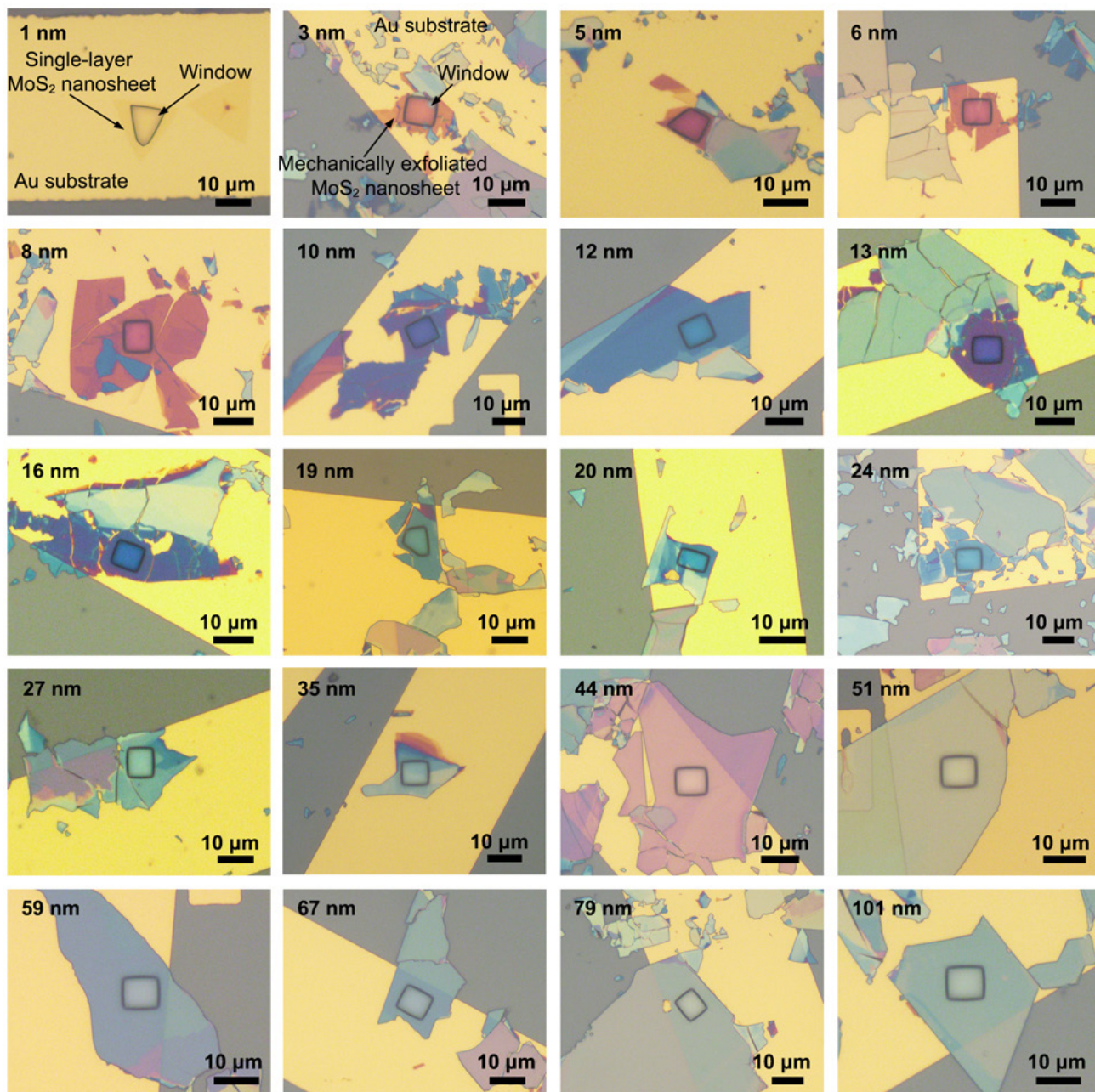
Figure S22. Optical images of micro-cells based on MoS₂ with thickness of 1-101 nm.

In order to examine the penetration depth of surface conductance, we fabricated a micro-cell, which can realize the vertical electron transport from the reaction interface to the bottom current collector (Au). The following **issues are carefully controlled to ensure the vertical electron transport**.

1. **The reaction window is only opened at the MoS₂ basal plane**. We only expose the basal plane region of MoS_2 nanosheet. Therefore, the carriers (electrons) are forced to transport vertically from the bottom Au contact to the catalyst surface. This is different from the conventional electrochemical cell with more charge transport pathways including the semiconductor edges and conductive additives.

2. **The active site density is controlled**. In order to enhance the electrochemical signal, we introduce the sulphur vacancy by Ar plasma, which can be identified from the attenuation of Raman signal[2], as shown in Figure S23a. In our experiment, such sulphur vacancy serves as active sites on the MoS_2 surface to improve the HER activity[2]. The resulting catalytic surface can be considered as a mixture of active sites (mostly S vacancies) and inert regions, which resembles the practical semiconductor catalyst surface according to our LMIS model (**Table S3**).

3. **Background current of each device is calibrated**. As shown in Figure S23b, the electrochemical current of MoS_2 decays rapidly with its thickness, giving a very weak electrochemical signal for the thick MoS_2. For example, the electrochemical current for 20-30 nm MoS_2 is only several nA. The background current of all devices is less than 0.1 nA (within the instrumental limit), which can be negligible during the electrochemical measurement (the inset of Figure S23b).
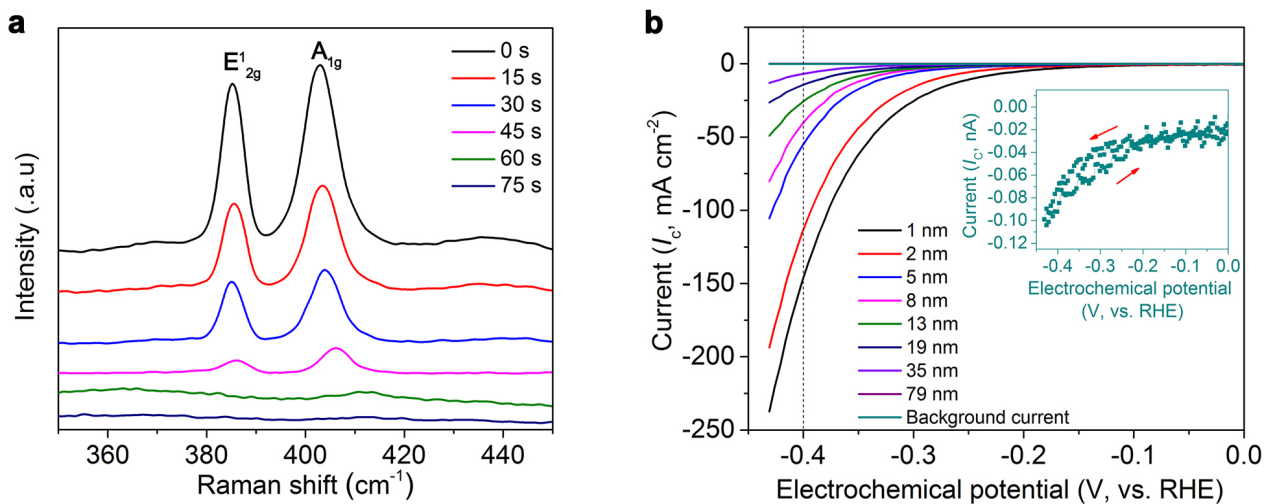
Figure S23. The HER measurement of micro-cells based on MoS₂ with different thickness. (a) Raman spectra of single-layer MoS$_2$ treated with Ar plasma for 0, 15, 30, 45, 60, and 70 s. The peaks at 386 and 404 cm^{-1} are assigned to the E^1_{2g} and A_{1g} modes, respectively. (b) Typical polarization curves of micro-cells based on MoS$_2$ with different thickness. Inset: Background current without the reaction window in the PMMA film.

Supplementary Note 4. Calculation of carrier density at the accumulation regime under self-gating
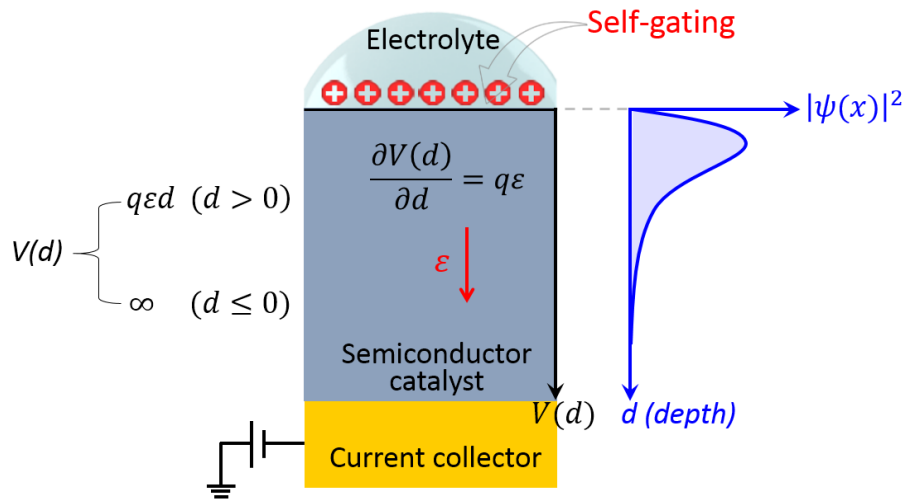
Figure S24. Distribution of carrier density in semiconductor catalyst under self-gating at anodic potential.

As shown in Figure S24, the effect of the self-gating on the carrier density in semiconductor catalyst can be considered as a triangular well with a constant electric field and an infinite barrier, given by,

$$V(d) = q\varepsilon d \ (d > 0) \tag{17}$$

$$or \ V(d) = \infty \ (d \leq 0) \tag{18}$$

where V is the potential energy, d is the depth beneath semiconductor surface, ε is the electric field strength, and q is a unit charge.

Time-independent Schrodinger's equation for the potential in equation (17) becomes:

$$\left[-\frac{\hbar^2}{2m}\frac{\partial^2}{\partial d^2} + q\varepsilon d\right]\psi(d) = E\psi(d) \tag{19}$$

where m is the mass of electron, V is the potential energy, d is the depth beneath semiconductor surface, ε is the electric field strength, q is a unit charge, ψ is the wave function, and E is the total energy of the system.

The Airy function is a solution to $\frac{d^2\psi}{ds^2} - s\psi = 0$, and approaches zero as d approaches infinity, in which s is given by $\left(\frac{2m}{h^2q^2\varepsilon^2}\right)^{1/3}(q\varepsilon d - E_n)$. As a result, the solution to the Schrödinger equation can be rewritten as:

$$\psi_n(d) = A \cdot Ai(s_n) = Ai\left[\left(\frac{2m}{h^2q^2\varepsilon^2}\right)^{1/3}(q\varepsilon d - E_n)\right] \tag{20}$$

where A is a proportionality constant which can be determined by normalization. Since $\psi(d = 0)$ has to be zero at the infinite barrier. According to equation,

$$\psi_n(0) = A \cdot Ai(s_0) = Ai\left[\left(\frac{2m}{h^2q^2\varepsilon^2}\right)^{1/3}(-E_n)\right] \tag{21}$$

the energy eigenvalues, E_n, are obtained from:

$$E_n = -\left(\frac{h^2q^2\varepsilon^2}{2m}\right)^{1/3} s_n \tag{22}$$

where s_n is the nth zero of the Airy function, i.e., $\left[\frac{3\pi(4n-1)}{8}\right]^{2/3}$. Therefore, the energy values can be finally rewritten as:

$$E_n \approx -\left(\frac{h^2q^2\varepsilon^2}{2m}\right)^{1/3}\left[\frac{3\pi(4n-1)}{8}\right]^{2/3} \tag{23}$$

where for n= 1, the first energy level can be obtained, i.e., $E_1 = \left(\frac{h^2}{2m}\right)^{1/3}\left[\frac{9\pi q\varepsilon}{8}\right]^{2/3}$.

Finally, the distribution of density of states ($|\psi|^2$) at first energy level can be given by,

$$|\psi_1(d)|^2 = \left|A \cdot Ai\left[\left(\frac{2m}{h^2q^2\varepsilon^2}\right)^{1/3}\left(q\varepsilon d - \left(\frac{h^2}{2m}\right)^{1/3}\left[\frac{9\pi q\varepsilon}{8}\right]^{2/3}\right)\right]\right|^2 \tag{24}$$

Based on the Supplementary Note 1, $d_{edl} \approx 0.34$ nm under positive electrochemical potential in 0.5 M H_2SO_4, the electrostatic field strength (ε) during the HER process is estimated to be about 1×10 MV cm^{-1}. According to the equation (24), we can plot the distribution of carrier density ($|\psi|^2$) along the thickness (d) of semiconductor catalyst in HER, as shown in Figure 3c.

Supplementary Note 5. Effect of the surface conductance on semiconductor catalysts

Semiconductors are commonly considered as non-ideal electrocatalysts due to their low conductance. For example, in a book titled "Electrocatalysis on Non-metallic Surfaces" authored by Alan D. Franklin"[33], the following two sentences are mentioned, *i.e.*, *No generalizing prediction can at present be made for the usefulness of non-metallic electrodes*, and *To some extent the conductivity problem can perhaps be overcome by using very thin layers on highly conductive substrates.*

In the electrocatalytic applications of semiconductors, additional conductive supports (*e.g.*, carbon additives)[50] are usually required to form composite electrodes. Therefore, for metallic electrocatalyst[51], the charge carrier can transport through its high conductive bulk. However, for semiconductor electrocatalyst[51], due to the low conductivity, the charge transfer process mainly occurs at the contact with its conductive support. However, this picture is difficult to explain the high activities of some recently reported semiconductor catalysts without conductive additives[3,52,53]. In our experiment, we found that self-gating could induce a charge transport pathway which renders the surface of semiconductors highly conductive. Such surface conductance can explain the high electrocatalytic activities of nanostructured semiconductor catalysts, *e.g.*, metal oxide[54-56] or 2D transition metal dichalcogenide[3,57,58] and previously reported semiconductor catalysts without conductive additives. Similar surface-conductance phenomenon was also observed in Li-air battery, in which the surface of insulating Li_2O_2 became metallic during its operation[59,60].

It is worth mentioning that the surface conductance plays an increasing important role as the dimensions of semiconductor catalysts are reduced from bulk to the nanometer scale. Such surface conductance can dominate the overall conductance of semiconductor catalysts under the self-gating, once their dimensions are reduced within the penetration depth of surface conductance (the

accumulation regime). In the last decade, shrinking of the dimensions from thin films to nanometer scale (or even to an atomic layer) has significantly improved the electrocatalytic performance, which is commonly explained by the increased surface area. Differently, we proved that the self-gating-induced surface conductance is a dominant factor for the increasing electrocatalytic performance of nanostructured semiconductors.

7 Correlation of the semiconductor types and the catalytic reactions

Figure S25a-c show the Si nanowires, fabricated via chemically etching the light-doped Si wafers with doping concentration of 10^{13} e cm^{-3}. The micro-cell fabrication is described in the Materials and Methods Section. Figure S25d, f, and g show the micro-cells of *n*-type, bipolar, and *p*-type Si nanowires, respectively. The similar self-gating phenomena with those observed in the aforementioned TMD micro-cells were also observed, *i.e.*, *n*-type Si nanowire exhibits HER activity as it is tuned on by the negative electrochemical potential under self-gating (Figure S25e), *p*-type one shows OER activity as it is tuned on by the positive electrochemical potential under self-gating (Figure S25g), and bipolar one shows both HER and OER activities as it is turned on by both negative and positive potentials under self-gating (Figure S25i).

Note that additional peaks before OER are observed, which may be related to the redox process of SiO$_x$. These peaks appear only after the *p*-type or bipolar Si nanowires are tuned on by the positive electrochemical potential, which is consistent with our aforementioned proposed principle. Finally, due to a small bandgap of Si (1.0-1.1 eV), the weak bipolar characteristics for both *n*-type and *p*-type Si nanowires under self-gating are observed (Figure S25e and i, red curves).
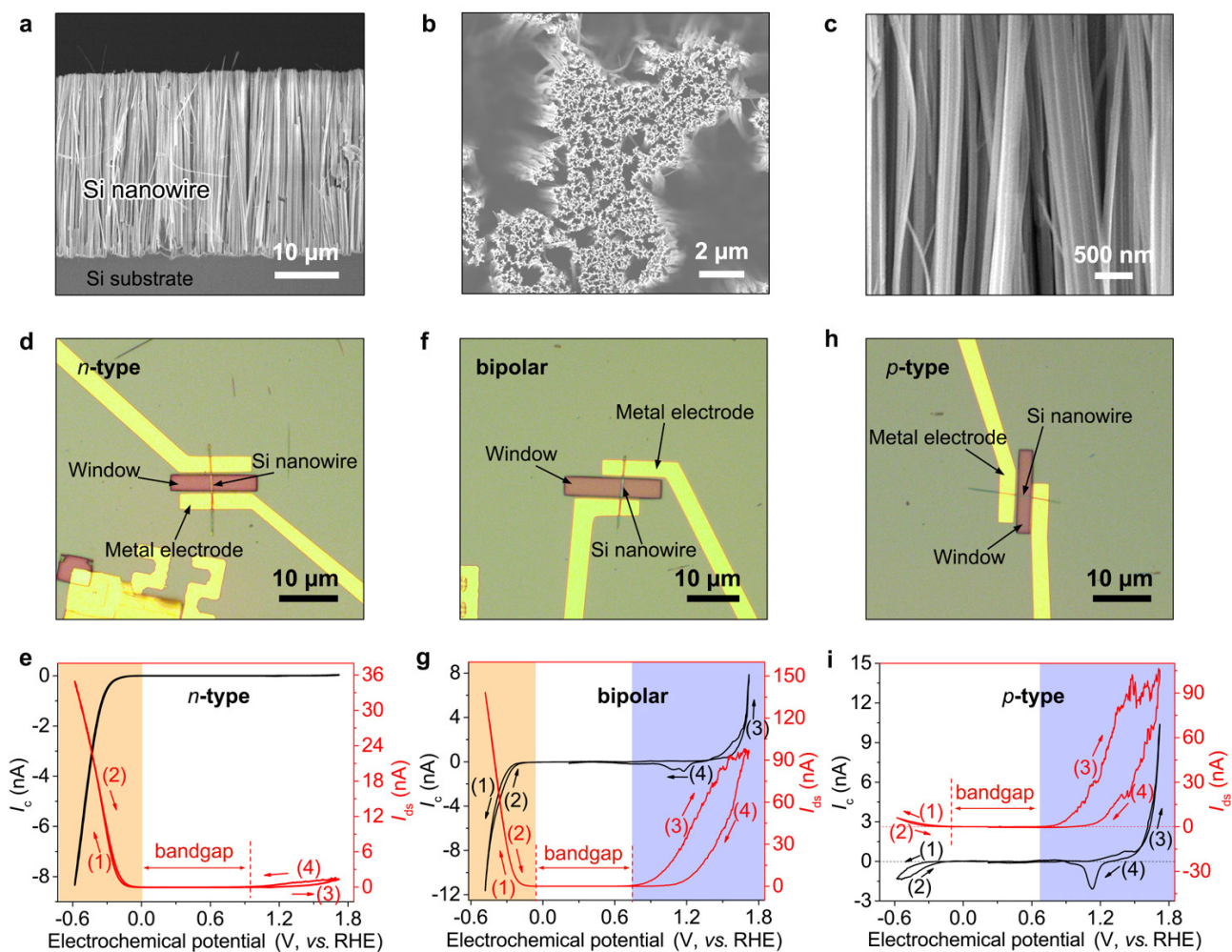
Figure S25. Self-gating on *n*-type, *p*-type and bipolar Si nanowires. (a)-(c) SEM images of the fabricated Si nanowires. (d)-(h) Optical images of *n*-type Si nanowire micro-cell (d), bipolar Si nanowire micro-cell (f), and *p*-type Si nanowire micro-cell (h). (e)-(i) *In-situ* electronic/electrochemical measurements of *n*-type Si nanowire (e), bipolar Si nanowire (g), and *p*-type Si nanowire (i).

Table S4. Correlation between the charge carrier types of previously studied semiconductors and their preferred electrocatalytic reactions (HER, OER, CO_2 reduction, and ORR).

Charge carrier	Semiconductor catalyst	Electrocatalytic reaction
n-type	MoS_2[61,62]*	HER[2,57,63-66]* and CO_2 reduction[67]
	$MoSe_2$[68]	HER[65,69]
	WS_2[70]	HER[4,71-73]
	WSe_2[74]	HER[75] and CO_2 reduction[76]
	ZnO[77]	CO_2 reduction[78]
	SnO_2[77]	CO_2 reduction[79]
	SnS_2[80]	HER[81]
	ReS_2[6]	HER[82,83]
	$MoTe_2$*	HER*
	$CoMoS_x$[84]	HER[85]
p-type	NiO[86,87]	ORR[88] and OER[89]
	$Ni(OH)_2$[90,91]	OER[92,93]
	CoO[94] and Co_3O_4[87,95]	ORR[55,96-101] and OER[55,97-100]
	$Co(OH)_2$[102]	OER[103,104]
	Cu_2O[105] and CuO[105,106]	ORR[107,108] and OER[109,110]
	Cu_2S[111]	OER[112]
	Mn_3O_4[113]	ORR[114] and OER[115]
	PtO_2[116]	OER[117]
	$NiCo_2O_4$[87]	ORR[118,119] and OER[96,120]
	$CuCo_2O_4$[121]	ORR[122] and OER[122]
	$MnCo_2O_4$[123]	ORR[124,125] and OER[124,125]
	Phosphorus-doped MoS_2[126]	ORR[127]
	WSe_2[128]	ORR[129]
	$WSe_{1.8}Te_{0.2}$[1]*	OER*
bipolar	Ta or Nb-doped MoS_2[126,130-132]	HER[133] and ORR[133]
	Ta or Nb-doped WS_2[131,132,134]	HER[133] and ORR[133]
	WSe_2[135]*	HER* and OER*

*Data collected in our experiments.

Note that some of VIA compound catalysts with high electrocatalytic performances are excluded in the table due to their metallic characteristics, such as metal chalcogenides (CoS_2[136,137], $CoSe_2$[138], NiS_2[136,139], $NiCo_2S_4$[140,141], VS_2[142], VTe_2[143], and $PtTe_2$[144]), and metal oxides[87] (RuO_2, RhO_2, IrO_2, $PtCoO_2$, and $PdXO_2$ (X=Co, Cr, or Rh)).

Supplementary Note 6. Discussions about Table S4

1. Metallic catalysts

Some of compound catalysts with high HER, OER, or CO_2 reduction performances are excluded in the Table S4 due to their metallic characteristics, such as metal chalcogenides (CoS_2[136,137], $CoSe_2$[138], NiS_2[136,139], $NiCo_2S_4$[140,141], VS_2[142], VTe_2[143], and $PtTe_2$[144]), and metal oxides[87] (RuO_2 and IrO_2). Note that some of them can also deliver a bifunctional electrocatalytic performances in both cathodic and anodic reactions (both HER and OER), such as NiS_2[139,145], $NiCo_2S_4$[140,141], $CoSe_2$[146,147], and Co_2P[148,149]. This is consistent with their metallic characteristics and the self-gating cannot affect their conductance. Interestingly, owing to the zero-gap band structure, graphene behaves like metal and remains highly conductive in all electrochemical windows, resulting in potentials for the electrocatalytic reactions in both positive and negative electrochemical windows.[150]

2. Weak self-gating at low electrochemical potentials

Some electrocatalytic reactions, such as HER, ORR, and CO_2 reduction, occur at a smaller electrochemical potential compared to OER. As a result, the strength of the self-gating in these electrocatalysis is relatively weak. Furthermore, other factors, such as synthetic methods, nanostructure varieties, defects, doping, *etc.*, will also affect the conductance of semiconductor catalysts. As a result, some *n*-type semiconductors, such as MoS_2[151,152] and $MoSe_2$[129] also deliver moderate ORR performance.

8 References

1   Yu, P. *et al.* Metal–Semiconductor Phase-Transition in WSe$_{2(1-x)}$Te$_{2x}$ Monolayer. *Adv. Mater.* **29**, 1603991 (2017).

2   Li, H. *et al.* Activating and optimizing MoS$_2$ basal planes for hydrogen evolution through the formation of strained sulphur vacancies. *Nat. Mater.* **15**, 48-53 (2016).

3   Voiry, D., Yang, J. & Chhowalla, M. Recent Strategies for Improving the Catalytic Activity of 2D TMD Nanosheets Toward the Hydrogen Evolution Reaction. *Adv. Mater.* **28**, 6197-6206 (2016).

4   Zhang, Y. *et al.* Chemical vapor deposition of monolayer WS$_2$ nanosheets on Au foils toward direct application in hydrogen evolution. *Nano Res.* **8**, 2881-2890 (2015).

5   Fritz Scholz, A. M. B., R.G. Compton, D.A. Fiedler, G. Inzelt, H. Kahlert, Š. Komorsky-Lovrić, H. Lohse, M. Lovrić, F. Marken, A. Neudeck, U. Retter, F. Scholz, Z. Stojek. *Electroanalytical Methods*. 2nd edn, Vol. 1 (Springer, 2010).

6   Liu, F. *et al.* Highly sensitive detection of polarized light using anisotropic 2D ReS$_2$. *Adv. Funct. Mater.* **26**, 1169-1177 (2016).

7   Yim, C. *et al.* High-performance hybrid electronic devices from layered PtSe$_2$ films grown at low temperature. *ACS Nano* **10**, 9550-9558 (2016).

8   Seh, Z. W. *et al.* Combining theory and experiment in electrocatalysis: Insights into materials design. *Science* **355** (2017).

9   Cho, S. *et al.* Phase patterning for ohmic homojunction contact in MoTe$_2$. *Science* **349**, 625-628 (2015).

10   Ji, Q. *et al.* Morphological engineering of CVD-grown transition metal dichalcogenides for efficient electrochemical hydrogen evolution. *Adv. Mater.* **28**, 6207-6212 (2016).

11   Ye, G. *et al.* Defects engineered monolayer MoS$_2$ for improved hydrogen evolution reaction. *Nano Lett.* **16**, 1097-1103 (2016).

12   Li, G. *et al.* All the catalytic active sites of MoS$_2$ for hydrogen evolution. *J. Am. Chem. Soc.* **138**, 16632-16638 (2016).

13   Voiry, D. *et al.* The role of electronic coupling between substrate and 2D MoS$_2$ nanosheets in electrocatalytic production of hydrogen. *Nat. Mater.* **15**, 1003-1009 (2016).

14   Zhang, J., Zhao, Z., Xia, Z. & Dai, L. A metal-free bifunctional electrocatalyst for oxygen reduction and oxygen evolution reactions. *Nat. Nanotechnol.* **10**, 444 (2015).

15   Bisquert, J. Influence of the boundaries in the impedance of porous film electrodes. *Phys. Chem. Chem. Phys.* **2**, 4185-4192 (2000).

16   Harrington, S. P. & Devine, T. M. Relation between the semiconducting properties of a passive film and reduction reaction rates. *J. Electrochem. Soc.* **156**, C154-C159 (2009).

17   Han, L. *et al.* Enhanced activity and acid pH stability of prussian blue-type oxygen evolution electrocatalysts processed by chemical etching. *J. Am. Chem. Soc.* **138**, 16037-16045 (2016).

18   Liu, X., Xiong, J., Lv, Y. & Zuo, Y. Study on corrosion electrochemical behavior of several different coating systems by EIS. *Prog. Org. Coat.* **64**, 497-503 (2009).

19   Mahdavian, M. & Attar, M. M. Another approach in analysis of paint coatings with EIS measurement: Phase angle at high frequencies. *Corros. Sci.* **48**, 4152-4157 (2006).

20   Pu, J. *et al.* Highly flexible MoS$_2$ thin-film transistors with ion gel dielectrics. *Nano Lett.* **12**, 4013-4017 (2012).

21   Chu, L. *et al.* Charge transport in ion-gated mono-, bi-, and trilayer MoS$_2$ field effect

transistors. *Sci. Rep.* **4**, 7293 (2014).

22   Pu, J. *et al.* Fabrication of stretchable MoS₂ thin-film transistors using elastic ion-gel gate dielectrics. *Appl. Phys. Lett.* **103**, 023505 (2013).

23   Zhang, Y., Ye, J., Matsuhashi, Y. & Iwasa, Y. Ambipolar MoS₂ Thin Flake Transistors. *Nano Lett.* **12**, 1136-1140 (2012).

24   Alves, V. A., da Silva, L. A. & Boodts, J. F. C. Surface characterisation of IrO₂/TiO₂/CeO₂ oxide electrodes and Faradaic impedance investigation of the oxygen evolution reaction from alkaline solution. *Electrochim. Acta* **44**, 1525-1534 (1998).

25   Vrubel, H., Moehl, T., Gratzel, M. & Hu, X. Revealing and accelerating slow electron transport in amorphous molybdenum sulphide particles for hydrogen evolution reaction. *Chem. Commun.* **49**, 8985-8987 (2013).

26   da Silva, L. A., Alves, V. A., da Silva, M. A. P., Trasatti, S. & Boodts, J. F. C. Oxygen evolution in acid solution on IrO₂+TiO₂ ceramic films. a study by impedance, voltammetry and SEM. *Electrochim. Acta* **42**, 271-281 (1997).

27   Morales-Guio, C. G., Liardet, L. & Hu, X. Oxidatively electrodeposited thin-film transition metal (oxy)hydroxides as oxygen evolution catalysts. *J. Am. Chem. Soc.* **138**, 8946-8957 (2016).

28   Doyle, R. L. & Lyons, M. E. G. An electrochemical impedance study of the oxygen evolution reaction at hydrous iron oxide in base. *Phys. Chem. Chem. Phys.* **15**, 5224-5237 (2013).

29   Morales-Guio, C. G. & Hu, X. Amorphous molybdenum sulfides as hydrogen evolution Catalysts. *Acc. Chem. Res.* **47**, 2671-2681 (2014).

30   Rajeshwar, K. *Fundamentals of Semiconductor Electrochemistry and Photoelectrochemistry*. Vol. 6 (Wiley-VCH, 2002).

31   Marcus, R. A. On the Theory of Oxidation-Reduction Reactions Involving Electron Transfer. I. *J. Chem. Phys.* **24**, 966-978 (1956).

32   Gerischer, H. Charge transfer processes at semiconductor-electrolyte interfaces in connection with problems of catalysis. *Surf. Sci.* **18**, 97-122 (1969).

33   Franklin, A. D. *Electrocatalysis on Non-Metallic Surfaces*. (National Bureau of Standards, 1975).

34   Nozik, A. J. & Memming, R. Physical Chemistry of Semiconductor−Liquid Interfaces. *J. Phys. Chem.* **100**, 13061-13078 (1996).

35   Allen J. Bard, L. R. F. *Electrochemical Methods: Fundamentals and Applications-2nd Edition*. (Wiley-VCH, 2000).

36   Akihiro, N., Masakazu, S., Katsushi, F. & Yoshiaki, N. Comparison of semiconductor–electrolyte and semiconductor–metal schottky junctions using AlGaN/GaN photoelectrochemical electrode. *Jpn. J. Appl. Phys.* **52**, 08JN20 (2013).

37   Neamen, D. *Semiconductor Physics And Devices*. (McGraw-Hill, Inc., 2003).

38   Lezama, I. G. *et al.* Single-crystal organic charge-transfer interfaces probed using Schottky-gated heterostructures. *Nat. Mater.* **11**, 788-794 (2012).

39   Kaji, T., Takenobu, T., Morpurgo, A. F. & Iwasa, Y. Organic single-crystal schottky gate transistors. *Adv. Mater.* **21**, 3689-3693 (2009).

40   Chhowalla, M., Jena, D. & Zhang, H. Two-dimensional semiconductors for transistors. *Nat. Rev. Mater.* **1**, 16052 (2016).

41   Ye, J. T. *et al.* Liquid-gated interface superconductivity on an atomically flat film. *Nat. Mater.*

9, 125-128 (2010).

42   Saito, Y. *et al.* Superconductivity protected by spin-valley locking in ion-gated MoS$_2$. *Nat. Phys.* **12**, 144-149 (2016).

43   Bisri, S. Z., Shimizu, S., Nakano, M. & Iwasa, Y. Endeavor of Iontronics: From Fundamentals to Applications of Ion-Controlled Electronics. *Adv. Mater.* **29**, 1607054 (2017).

44   Fang, H. & Hu, W. Photogating in Low Dimensional Photodetectors. *Adv. Sci.* **4**, 1700323 (2017).

45   Adinolfi, V. & Sargent, E. H. Photovoltage field-effect transistors. *Nature* **542**, 324 (2017).

46   Furchi, M. M., Polyushkin, D. K., Pospischil, A. & Mueller, T. Mechanisms of Photoconductivity in Atomically Thin MoS$_2$. *Nano Lett.* **14**, 6165-6170 (2014).

47   Hai, H. *et al.* Highly sensitive visible to infrared MoTe$_2$ photodetectors enhanced by the photogating effect. *Nanotechnology* **27**, 445201 (2016).

48   Ye, Y. *et al.* High-Performance Single CdS Nanobelt Metal-Semiconductor Field-Effect Transistor-Based Photodetectors. *ACS Appl. Mater. Interfaces* **2**, 2724-2727 (2010).

49   Shin, H. G. *et al.* Vertical and In-Plane Current Devices Using NbS$_2$/n-MoS$_2$ van der Waals Schottky Junction and Graphene Contact. *Nano Lett.* **18**, 1937-1945 (2018).

50   Raccichini, R., Varzi, A., Passerini, S. & Scrosati, B. The role of graphene for electrochemical energy storage. *Nat. Mater.* **14**, 271 (2014).

51   Xu, Z. J. From Two-Phase to Three-Phase: The New Electrochemical Interface by Oxide Electrocatalysts. *Nano-Micro Lett.* **10**, 8 (2017).

52   Burke, M. S., Kast, M. G., Trotochaud, L., Smith, A. M. & Boettcher, S. W. Cobalt–Iron (Oxy)hydroxide Oxygen Evolution Electrocatalysts: The Role of Structure and Composition on Activity, Stability, and Mechanism. *J. Am. Chem. Soc.* **137**, 3638-3648 (2015).

53   Trotochaud, L., Young, S. L., Ranney, J. K. & Boettcher, S. W. Nickel–Iron Oxyhydroxide Oxygen-Evolution Electrocatalysts: The Role of Intentional and Incidental Iron Incorporation. *J. Am. Chem. Soc.* **136**, 6744-6753 (2014).

54   Suntivich, J., May, K. J., Gasteiger, H. A., Goodenough, J. B. & Shao-Horn, Y. A Perovskite Oxide Optimized for Oxygen Evolution Catalysis from Molecular Orbital Principles. *Science* **334**, 1383-1385 (2011).

55   Liang, Y. *et al.* Co$_3$O$_4$ nanocrystals on graphene as a synergistic catalyst for oxygen reduction reaction. *Nat. Mater.* **10**, 780-786 (2011).

56   Chao, W. *et al.* Cations in Octahedral Sites: A Descriptor for Oxygen Electrocatalysis on Transition-Metal Spinels. *Adv. Mater.* **29**, 1606800 (2017).

57   Jaramillo, T. F. *et al.* Identification of active edge sites for electrochemical H$_2$ evolution from MoS$_2$ nanocatalysts. *Science* **317**, 100-102 (2007).

58   Liu, Y. *et al.* Self-optimizing, highly surface-active layered metal dichalcogenide catalysts for hydrogen evolution. *Nat. Energy* **2**, 17127 (2017).

59   Hummelshøj, J. S. *et al.* Communications: Elementary oxygen electrode reactions in the aprotic Li-air battery. *J. Chem. Phys.* **132**, 071101 (2010).

60   Viswanathan, V. *et al.* Electrical conductivity in Li$_2$O$_2$ and its role in determining capacity limitations in non-aqueous Li-O$_2$ batteries. *J. Chem. Phys.* **135**, 214704 (2011).

61   Das, S., Chen, H.-Y., Penumatcha, A. V. & Appenzeller, J. High performance multilayer MoS$_2$ transistors with scandium contacts. *Nano Lett.* **13**, 100-105 (2013).

62   RadisavljevicB, RadenovicA, BrivioJ, GiacomettiV & KisA. Single-layer MoS$_2$ transistors.

Nat. Nanotechnol. **6**, 147-150 (2011).

63   Li, Y. *et al.* MoS₂ nanoparticles grown on graphene: an advanced catalyst for the hydrogen evolution reaction. *J. Am. Chem. Soc.* **133**, 7296-7299 (2011).

64   Kibsgaard, J., Chen, Z., Reinecke, B. N. & Jaramillo, T. F. Engineering the surface structure of MoS₂ to preferentially expose active edge sites for electrocatalysis. *Nat. Mater.* **11**, 963-969 (2012).

65   Kong, D. *et al.* Synthesis of MoS₂ and MoSe₂ films with vertically aligned layers. *Nano Lett.* **13**, 1341-1347 (2013).

66   Deng, J. *et al.* Multiscale structural and electronic control of molybdenum disulfide foam for highly efficient hydrogen production. *Nat. Commun.* **8**, 14430 (2017).

67   Asadi, M. *et al.* Robust carbon dioxide reduction on molybdenum disulphide edges. *Nat. Commun.* **5**, 4470 (2014).

68   Wang, X. *et al.* Chemical vapor deposition growth of crystalline monolayer MoSe₂. *ACS Nano* **8**, 5125-5131 (2014).

69   Saadi, F. H. *et al.* Operando synthesis of macroporous molybdenum diselenide films for electrocatalysis of the hydrogen-evolution reaction. *ACS Catal.* **4**, 2866-2873 (2014).

70   Huo, N. *et al.* Photoresponsive and gas sensing field-effect transistors based on multilayer WS₂ nanoflakes. *Sci. Rep.* **4**, 5209 (2014).

71   Cheng, L. *et al.* Ultrathin WS₂ nanoflakes as a high-performance electrocatalyst for the hydrogen evolution reaction. *Angew. Chem. Int. Ed.* **53**, 7860-7863 (2014).

72   Duan, J., Chen, S., Chambers, B. A., Andersson, G. G. & Qiao, S. Z. 3D WS₂ nanolayers@heteroatom-doped graphene films as hydrogen evolution catalyst electrodes. *Adv. Mater.* **27**, 4234-4241 (2015).

73   Choi, C. L. *et al.* WS₂ nanoflakes from nanotubes for electrocatalysis. *Nano Res.* **6**, 921-928 (2013).

74   Liu, W. *et al.* Role of metal contacts in designing high-performance monolayer n-type WSe₂ field effect transistors. *Nano Lett.* **13**, 1983-1990 (2013).

75   Liu, Z. *et al.* Assembled 3D electrocatalysts for efficient hydrogen evolution: WSe₂ layers anchored on graphene sheets. *Inorg. Chem. Front.* **3**, 313-319 (2016).

76   Asadi, M. *et al.* Nanostructured transition metal dichalcogenide electrocatalysts for CO₂ reduction in ionic liquid. *Science* **353**, 467-470 (2016).

77   Rödl, C. & Schleife, A. Photoemission spectra and effective masses of n- and p-type oxide semiconductors from first principles: ZnO, CdO, SnO₂, MnO, and NiO. *Phys. Status solidi A* **211**, 74-81 (2014).

78   Jiang, X. *et al.* Electrocatalytic reduction of carbon dioxide over reduced nanoporous zinc oxide. *Electrochem. Commun.* **68**, 67-70 (2016).

79   Li, F., Chen, L., Knowles, G. P., MacFarlane, D. R. & Zhang, J. Hierarchical mesoporous SnO₂ nanosheets on carbon cloth: a robust and flexible electrocatalyst for CO₂ reduction with high efficiency and selectivity. *Angew. Chem.* **129**, 520-524 (2017).

80   Ahn, J.-H. *et al.* Deterministic two-dimensional polymorphism growth of hexagonal n-type SnS₂ and orthorhombic p-type SnS crystals. *Nano Lett.* **15**, 3703-3708 (2015).

81   Chia, X., Lazar, P., Sofer, Z., Luxa, J. & Pumera, M. Layered SnS *versus* SnS₂: valence and structural implications on electrochemistry and clean energy electrocatalysis. *J. Phys. Chem. C* **120**, 24098-24111 (2016).

82   Gao, J. *et al.* Vertically oriented arrays of ReS_2 nanosheets for electrochemical energy storage and electrocatalysis. *Nano Lett.* **16**, 3780-3787 (2016).

83   Fujita, T. *et al.* Chemically exfoliated ReS_2 nanosheets. *Nanoscale* **6**, 12458-12462 (2014).

84   Li, B. *et al.* Synthesis and transport properties of large-scale alloy $Co_{0.16}Mo_{0.84}S_2$ bilayer nanosheets. *ACS Nano* **9**, 1257-1262 (2015).

85   Staszak-Jirkovsky, J. *et al.* Design of active and stable Co-Mo-S_x chalcogels as pH-universal catalysts for the hydrogen evolution reaction. *Nat. Mater.* **15**, 197-203 (2016).

86   Sato, H., Minami, T., Takata, S. & Yamada, T. Transparent conducting p-type NiO thin films prepared by magnetron sputtering. *Thin Solid Films* **236**, 27-31 (1993).

87   Matsumoto, Y. & Sato, E. Electrocatalytic properties of transition metal oxides for oxygen evolution reaction. *Mater. Chem. Phys.* **14**, 397-426 (1986).

88   Huang, J. *et al.* Nickel oxide and carbon nanotube composite (NiO/CNT) as a novel cathode non-precious metal catalyst in microbial fuel cells. *Biosens. Bioelectron.* **72**, 332-339 (2015).

89   Wang, J. *et al.* Synergistic effect between metal–nitrogen–carbon sheets and NiO nanoparticles for enhanced electrochemical water-oxidation performance. *Angew. Chem. Int. Ed.* **54**, 10530-10534 (2015).

90   Tkalych, A. J., Yu, K. & Carter, E. A. Structural and electronic features of β-$Ni(OH)_2$ and β-NiOOH from first principles. *J. Phys. Chem. C* **119**, 24315-24322 (2015).

91   Patil, U. M., Gurav, K. V., Fulari, V. J., Lokhande, C. D. & Joo, O. S. Characterization of honeycomb-like "β-$Ni(OH)_2$" thin films synthesized by chemical bath deposition method and their supercapacitor application. *J. Power Sources* **188**, 338-342 (2009).

92   Zhou, X., Xia, Z., Zhang, Z., Ma, Y. & Qu, Y. One-step synthesis of multi-walled carbon nanotubes/ultra-thin $Ni(OH)_2$ nanoplate composite as efficient catalysts for water oxidation. *J. Mater. Chem. A* **2**, 11799-11806 (2014).

93   Stern, L.-A. & Hu, X. Enhanced oxygen evolution activity by NiO_x and $Ni(OH)_2$ nanoparticles. *Faraday Discuss.* **176**, 363-379 (2014).

94   Koel, G. J. & Gellings, P. J. The contribution of different types of point defects to diffusion in CoO and NiO during oxidation of the metals. *Oxid. Met.* **5**, 185-203 (1972).

95   Zhang, H. *et al.* PdO doping tunes band-gap energy levels as well as oxidative stress responses to a Co_3O_4 p-type semiconductor in cells and the lung. *J. Am. Chem. Soc.* **136**, 6406-6420 (2014).

96   Chen, S. & Qiao, S.-Z. Hierarchically porous nitrogen-doped graphene–$NiCo_2O_4$ hybrid paper as an advanced electrocatalytic water-splitting material. *ACS Nano* **7**, 10190-10196 (2013).

97   Li, X. *et al.* MOF derived Co_3O_4 nanoparticles embedded in N-doped mesoporous carbon layer/MWCNT hybrids: extraordinary bi-functional electrocatalysts for OER and ORR. *J. Mater. Chem. A* **3**, 17392-17402 (2015).

98   Mao, S., Wen, Z., Huang, T., Hou, Y. & Chen, J. High-performance bi-functional electrocatalysts of 3D crumpled graphene-cobalt oxide nanohybrids for oxygen reduction and evolution reactions. *Energy Environ. Sci.* **7**, 609-616 (2014).

99   Zhang, X. *et al.* Co/CoO nanoparticles immobilized on Co-N-doped carbon as trifunctional electrocatalysts for oxygen reduction, oxygen evolution and hydrogen evolution reactions. *Chem. Commun.* **52**, 5946-5949 (2016).

100   Jiang, Z.-J. & Jiang, Z. Interaction induced high catalytic activities of CoO nanoparticles

grown on nitrogen-doped hollow graphene microspheres for oxygen reduction and evolution reactions. *Sci. Rep.* **6**, 27081 (2016).

101   Liang, Y. *et al.* Oxygen reduction electrocatalyst based on strongly coupled cobalt oxide nanocrystals and carbon nanotubes. *J. Am. Chem. Soc.* **134**, 15849-15857 (2012).

102   Santamaria, M., Adragna, E. & Di Quarto, F. Identification of passive layers on Co in alkaline solutions by photocurrent spectroscopy. *Electrochem. Solid-State Lett.* **8**, B12-B15 (2005).

103   Jiang, Y., Li, X., Wang, T. & Wang, C. Enhanced electrocatalytic oxygen evolution of α-$Co(OH)_2$ nanosheets on carbon nanotube/polyimide films. *Nanoscale* **8**, 9667-9675 (2016).

104   Gao, Y. Q., Li, H. B. & Yang, G. W. Amorphous $Co(OH)_2$ nanosheet electrocatalyst and the physical mechanism for its high activity and long-term cycle stability. *J. Appl. Phys.* **119**, 034902 (2016).

105   Heinemann, M., Eifert, B. & Heiliger, C. Band structure and phase stability of the copper oxides Cu_2O, CuO, and Cu_4O_3. *Phys. Rev. B* **87**, 115111 (2013).

106   *Copper(II) oxide: a p-type semiconductor* <https://en.wikipedia.org/wiki/Copper(II)_oxide> (2017).

107   Zhou, R., Zheng, Y., Hulicova-Jurcakova, D. & Qiao, S. Z. Enhanced electrochemical catalytic activity by copper oxide grown on nitrogen-doped reduced graphene oxide. *J. Mater. Chem. A* **1**, 13179-13185 (2013).

108   Xu, Y. *et al.* Conversion of CuO nanoplates into porous hybrid Cu_2O/polypyrrole nanoflakes through a pyrrole-induced reductive transformation reaction. *Chem. Asian J.* **8**, 1120-1127 (2013).

109   Liu, X. *et al.* Self-supported copper oxide electrocatalyst for water oxidation at low overpotential and confirmation of its robustness by Cu K-edge X-ray absorption spectroscopy. *J. Phys. Chem. C* **120**, 831-840 (2016).

110   Li, Q. *et al.* Structure-dependent electrocatalytic properties of Cu_2O nanocrystals for oxygen reduction reaction. *J. Phys. Chem. C* **117**, 13872-13878 (2013).

111   Wong, A. B., Brittman, S., Yu, Y., Dasgupta, N. P. & Yang, P. Core–shell CdS–Cu_2S nanorod array solar cells. *Nano Lett.* **15**, 4096-4101 (2015).

112   An, L. *et al.* Phase transformation fabrication of a Cu_2S nanoplate as an efficient catalyst for water oxidation with glycine. *Inorg. Chem.* **54**, 3281-3289 (2015).

113   Kim, H.-J. & Lee, J.-H. Highly sensitive and selective gas sensors using p-type oxide semiconductors: Overview. *Sensor. Actuat. B-Chem.* **192**, 607-627 (2014).

114   Bag, S., Roy, K., Gopinath, C. S. & Raj, C. R. Facile single-step synthesis of nitrogen-doped reduced graphene oxide-Mn_3O_4 hybrid functional material for the electrocatalytic reduction of oxygen. *ACS Appl. Mater. Interfaces* **6**, 2692-2699 (2014).

115   Gao, M.-R., Xu, Y.-F., Jiang, J., Zheng, Y.-R. & Yu, S.-H. Water oxidation electrocatalyzed by an efficient Mn_3O_4/$CoSe_2$ nanocomposite. *J. Am. Chem. Soc.* **134**, 2930-2933 (2012).

116   Yang, Y., Sugino, O. & Ohno, T. Possible magnetic behavior in oxygen-deficient β-PtO_2. *Phys. Rev. B* **85**, 035204 (2012).

117   Gao, M.-R. *et al.* Completely green synthesis of colloid adams' catalyst α-PtO_2 nanocrystals and derivative Pt nanocrystals with high activity and stability for oxygen reduction. *Chem. Eur. J.* **18**, 8423-8429 (2012).

118   Zhang, G., Xia, B. Y., Wang, X. & Lou, X. W. Strongly coupled $NiCo_2O_4$-rGO hybrid nanosheets as a methanol-tolerant electrocatalyst for the oxygen reduction reaction. *Adv.*

Mater. **26**, 2408-2412 (2014).

119   Xiao, Y., Hu, C., Qu, L., Hu, C. & Cao, M. Three-dimensional macroporous $NiCo_2O_4$ sheets as a non-noble catalyst for efficient oxygen reduction reactions. *Chem. Eur. J.* **19**, 14271-14278 (2013).

120   Cui, B. *et al.* Core-ring structured $NiCo_2O_4$ nanoplatelets: synthesis, characterization, and electrocatalytic applications. *Adv. Funct. Mater.* **18**, 1440-1447 (2008).

121   Alizadeh-Gheshlaghi, E., Shaabani, B., Khodayari, A., Azizian-Kalandaragh, Y. & Rahimi, R. Investigation of the catalytic activity of nano-sized CuO, Co_3O_4 and $CuCo_2O_4$ powders on thermal decomposition of ammonium perchlorate. *Powder Technol.* **217**, 330-339 (2012).

122   Serov, A. *et al.* $CuCo_2O_4$ ORR/OER bi-functional catalyst: influence of synthetic approach on performance. *J. Electrochem. Soc.* **162**, F449-F454 (2015).

123   Vakiv, M., Hadzaman, I., Klym, H., Shpotyuk, O. & Brunner, M. Multifunctional thick-film structures based on spinel ceramics for environment sensors. *J. Phys: Conf. Ser.* **289**, 012011 (2011).

124   Ge, X. *et al.* Dual-phase spinel $MnCo_2O_4$ and spinel $MnCo_2O_4$/nanocarbon hybrids for electrocatalytic oxygen reduction and evolution. *ACS Appl. Mater. Interfaces* **6**, 12684-12691 (2014).

125   Cao, X. *et al.* Electrochemical properties of $MnCo_2O_4$ spinel bifunctional catalyst for oxygen reduction and evolution reaction. *J. Electrochem. Soc.* **161**, H296-H300 (2014).

126   Nipane, A., Karmakar, D., Kaushik, N., Karande, S. & Lodha, S. Few-layer MoS_2 p-type devices enabled by selective doping using low energy phosphorus implantation. *ACS Nano* **10**, 2128-2137 (2016).

127   Huang, H., Feng, X., Du, C. & Song, W. High-quality phosphorus-doped MoS_2 ultrathin nanosheets with amenable ORR catalytic activity. *Chem. Commun.* **51**, 7903-7906 (2015).

128   Zhou, H. *et al.* Large area growth and electrical properties of p-type WSe_2 atomic layers. *Nano Lett.* **15**, 709-713 (2015).

129   Guo, J., Shi, Y., Bai, X., Wang, X. & Ma, T. Atomically thin $MoSe_2$/graphene and WSe_2/graphene nanosheets for the highly efficient oxygen reduction reaction. *J. Mater. Chem. A* **3**, 24397-24404 (2015).

130   Suh, J. *et al.* Doping against the native propensity of MoS_2: degenerate hole doping by cation substitution. *Nano Lett.* **14**, 6976-6982 (2014).

131   Tedstone, A. A., Lewis, D. J. & O'Brien, P. Synthesis, properties, and applications of transition metal-doped layered transition metal dichalcogenides. *Chem. Mater.* **28**, 1965-1974 (2016).

132   Aram, Y. & and Zonghoon, L. Synthesis and properties of two dimensional doped transition metal dichalcogenides. *Appl. Microsc.* **47**, 19-28 (2017).

133   Chua, X. J. *et al.* Negative electrocatalytic effects of p-doping niobium and tantalum on MoS_2 and WS_2 for the hydrogen evolution reaction and oxygen reduction reaction. *ACS Catal.* **6**, 5724-5734 (2016).

134   Duan, X. *et al.* Synthesis of $WS_{2x}Se_{2-2x}$ alloy nanosheets with composition-tunable electronic properties. *Nano Lett.* **16**, 264-269 (2016).

135   Agnihotri, P., Dhakras, P. & Lee, J. U. Bipolar junction transistors in two-dimensional WSe_2 with large current and photocurrent gains. *Nano Lett.* **16**, 4355-4360 (2016).

136   Pearce, C. I., Pattrick, R. A. D. & Vaughan, D. J. Electrical and magnetic properties of

sulfides. *Rev. Mineral. Geochem.* **61**, 127-180 (2006).

137   Faber, M. S. *et al.* High-performance electrocatalysis using metallic cobalt pyrite (CoS_2) micro- and nanostructures. *J. Am. Chem. Soc.* **136**, 10053-10061 (2014).

138   Kong, D., Wang, H., Lu, Z. & Cui, Y. $CoSe_2$ nanoparticles grown on carbon fiber paper: an efficient and stable electrocatalyst for hydrogen evolution reaction. *J. Am. Chem. Soc.* **136**, 4897-4900 (2014).

139   Wang, J. *et al.* NiS_2 nanosheet array: A high-active bifunctional electrocatalyst for hydrazine oxidation and water reduction toward energy-efficient hydrogen production. *Mater. Today Energy* **3**, 9-14 (2017).

140   Xia, C., Li, P., Gandi, A. N., Schwingenschlögl, U. & Alshareef, H. N. Is $NiCo_2S_4$ really a semiconductor? *Chem. Mater.* **27**, 6482-6485 (2015).

141   Sivanantham, A., Ganesan, P. & Shanmugam, S. Hierarchical $NiCo_2S_4$ nanowire arrays supported on Ni foam: an efficient and durable bifunctional electrocatalyst for oxygen and hydrogen evolution reactions. *Adv. Funct. Mater.* **26**, 4661-4672 (2016).

142   Yuan, J. *et al.* Facile synthesis of single crystal vanadium sisulfide nanosheets by chemical vapor deposition for efficient hydrogen evolution reaction. *Adv. Mater.* **27**, 5605-5609 (2015).

143   Chia, X., Ambrosi, A., Lazar, P., Sofer, Z. & Pumera, M. Electrocatalysis of layered Group 5 metallic transition metal dichalcogenides (MX_2, M = V, Nb, and Ta; X = S, Se, and Te). *J. Mater. Chem. A* **4**, 14241-14253 (2016).

144   Chia, X. *et al.* Layered platinum dichalcogenides (PtS_2, $PtSe_2$, and $PtTe_2$) electrocatalysis: monotonic dependence on the chalcogen size. *Adv. Funct. Mater.* **26**, 4306-4318 (2016).

145   Chen, G.-F. *et al.* Efficient and stable bifunctional electrocatalysts Ni/Ni_xM_y (M = P, S) for overall water splitting. *Adv. Funct. Mater.* **26**, 3314-3323 (2016).

146   Sun, C. *et al.* Metal–organic framework derived $CoSe_2$ nanoparticles anchored on carbon fibers as bifunctional electrocatalysts for efficient overall water splitting. *Nano Res.* **9**, 2234-2243 (2016).

147   Li, K., Zhang, J., Wu, R., Yu, Y. & Zhang, B. Anchoring CoO domains on $CoSe_2$ nanobelts as bifunctional electrocatalysts for overall water splitting in neutral media. *Adv. Sci.* **3**, 1500426 (2016).

148   Jin, Z., Li, P. & Xiao, D. Metallic Co_2P ultrathin nanowires distinguished from CoP as robust electrocatalysts for overall water-splitting. *Green Chem.* **18**, 1459-1464 (2016).

149   Jiang, H. *et al.* Supramolecular gel-assisted synthesis Co_2P particles anchored in multielement co-doped graphene as efficient bifunctional electrocatalysts for oxygen reduction and evolution. *Electrochim. Acta* **231**, 344-353 (2017).

150   Liu, X. & Dai, L. Carbon-based metal-free catalysts. *Nat. Rev. Mater.* **1**, 16064 (2016).

151   Wang, T. *et al.* Synergistic catalytic effect of MoS_2 nanoparticles supported on gold nanoparticle films for a highly efficient oxygen reduction reaction. *ChemCatChem* **6**, 1877-1881 (2014).

152   Wang, T. *et al.* Size-dependent enhancement of electrocatalytic oxygen-reduction and hydrogen-evolution performance of MoS_2 particles. *Chem. Eur. J.* **19**, 11939-11948 (2013).